이학박사 학위논문

First-principles Study of Electronic, Magnetic, and Topological Properties of 2-Dimensional Kagome Metal-Organic Frameworks

2차원 카고메 금속유기화합물의 전기, 자성 및 위상학적 성질에 대한 연구

2022 년 8 월

서울대학교 대학원

물리천문학부

강 승 진

First-principles Study of Electronic, Magnetic, and Topological Properties of 2-Dimensional Kagome Metal-Organic Frameworks

2차원 카고메 금속유기화합물의 전기, 자성 및 위상학적 성질에 대한 연구

지도교수 유 재 준

이 논문을 이학박사 학위논문으로 제출함

2022 년 7 월

서울대학교 대학원

물리천문학부

강 승 진

강승진의 이학박사 학위논문을 인준함

2022 년 7 월

위 원 장 박 제 근 (인)

부위원장 유 재 준 (인)

위 원 김 기 훈 (인)

위 원 양 범 정 (인)

위 원 김 흥 식 (인)

Abstract

Advnaces on experimental technique have lead researchers to study various kinds of two-dimensional (2D) materials. Among various 2D materials, metal-organic frameworks (MOFs) are being considered as a new class of materials where 2D properties can be ideally studied. The knowledge of coordination chemistry enables us to tune the target properties of intersts by choosing proper ligands. Experiments especially suggest that some kagome MOFs can host ferromagnetism, quantum anomalous Hall effect, or spin liquid behavior. However, implementing magnetic properties in MOFs is ususally challenging because distinct ligands can result in a different magnetic behavior even with the same metal atoms. Thus, it is necessary to develop some general picture of understanding how these ligand states affect the electronic and magnetic properties on MOFs. In this thesis, we establish a general picture of understanding the magnetic and topological properties of 2D kagome MOFs. From first-principles calculations, we determine their crystal structure, magnetic ground states, anisotropy, and topological properties on a series of transition metal atoms and ligands. We show that metal-ligand hybridization is the vital feature in the electronic structure of MOFs and identify the primary mechanism for magnetic ordering in 2D kagome MOFs. Topological properties also depend on the metal-ligand hybridization and we show how the quantum phase transition can be controlled.

Keywords: metal-organic frameworks, kagome lattice, magnetic coupling, Chern insulator

Student Number: 2013-22981

Contents

List of Figures

List of Tables

Chapter 1

Introduction

Two-dimensional (2D) materials have attracted great interest in recent years. Initiated by the synthesis of monolayer graphene, various 2D materials have been studied [1, 2, 3, 4]. They provide high conductivity, strong mechanical stability, and versatile tuning possibilities.

Having established some fundamental understanding of these graphene-based 2D systems, researchers have been looking for post-graphene systems. One of these post-graphene research areas is introducing magnetism to 2D materials. Among various candidates, the layered van der Waals (vdW) materials have attracted much interest due to their easy exfoliation properties[5]. They contain transition metal (TM) atoms, so magnetic moments by d electrons can be easily induced. Researchers have observed various magnetic behavior on these vdW materials. Cr-based chalcogenides (CrI_3, $Cr_2Ge_2Te_6$, $CrCl_3$) show FM behavior in the monolayer limit[6, 7, 8]. $TMPX_3$-type materials exhibit plethora of magnetic interaction such as Ising($FePS_3$), Heisenberg($MnPS_3$), or XY($NiPS_3$) interaction depending on the

metal constituent[9, 10, 11]. Other vdW materials such as dihalides (FeX_2, NiX_2) or trihalides($RuCl_3$) also show exotic magnetic properties[12, 13, 14].

The discovery of magnetism in the 2D limit was intriguing because it has long been believed that the long-range order in the 2D system is usually suppressed due to Mermin–Wagner theorem. Weak signals in the 2D system also hindered the study of magnetism in 2D materials. However, it has been suggested that the spin-orbit coupling (SOC) could provide sufficient magnetic anisotropy to overcome the Mermin-Wagner constraint. The advance in experimental techniques such as the magneto-optic Kerr effect (MOKE) has also made it possible to detect the weak magnetic signal in a 2D system. The discovery of magnetic behavior in these representative systems has triggered the study of 2D magnetic materials. Stimulated by this, scientists have studied various magnetic properties on 2D magnetic materials both on experimental and theoretical sides[15, 16, 17, 18, 19, 20, 21, 22].

However, some difficulties exist in utilizing these vdW-based magnetic materials for further applications. One of the significant challenges in TM chalcogenides or halides is the isolation of the mono or few layers from their bulk counterparts to study the 2D behavior[23]. These materials are usually prepared by exfoliation from the layered inorganic materials connected by weak vdW interaction. The chemical instability after exfoliation and low yield are the major bottlenecks limiting their applicability[24, 25]. Although the exfoliation method, so-called the top-down approach where one starts from the bulk and exfoliates them, has the advantage of obtaining clean and good crystalline nanosheets, overcoming the low yield and stability issue is challenging.

There is another approach to preparing the nanosheet sample, called bottom-up synthesis. In this approach, the desired nanosheet sample is directly synthesized

from the metal ions and their linkers[26]. With a suitable choice of synthesis conditions, one can block the growth of the sample along the out-of-plane direction and control the layer width in the desired manner. This approach requires the sophisticated control of the chemical reactions between metal and the linkers. One widely studied material employing this bottom-up synthesis technique is the metal-organic frameworks (MOFs) systems.

MOFs are metal ions or clusters coordinated to organic linkers (phosphonates, carboxylates). The strong coordination bond between metal and ligands provides high stability to the MOFs system[27]. Various knowledge from organic chemistry also enables us to apply the bottom-up approach to grow the sample to nanosheets. Due to these advantages in both synthesis process and chemical stability, MOFs are considered a new platform for studying 2D properties[28, 29]. Although the main interests in MOFs are conventionally concentrated on the application sides, such as energy storage, catalysis, or sensors[30], they could provide a suitable platform for studying 2D magnetism.

Recent studies suggest that magnetism can also be realized in 2D MOFs. It has been reported that the localized magnetic moments of Fe atoms can survive and possibly contribute to the quantum anomalous Hall effect (QAHE)[31, 32]. It has also been reported that Fe-based MOFs with coronene as a linker show FM behavior[33]. Another 2D MOFs with hexaaminobenzene (HAB) or hexaiminotriphenylene (HITP) could also be a candidate for magnetic MOFs[34, 35]. It has been suggested employing magnetic MOFs for spintronics[36, 37], magnetoelectric materials[38], and magnetic semiconductors[39]. On the theoretical side, various interesting issues on magnetic MOFs exist. It has been suggested that MOFs of $M_3(C_6O_6)_2$-type could exhibit double Dirac cones feature and give a sizable QAHE

signal by tuning the Fermi level[40]. There also exist extensive calculations of the general properties of 2D MOFs on kagome lattice[41, 42].

One of the advantages of MOFs over other 2D chalcogenides and halides materials is the tunability of physical properties. With a proper choice of organic linkers, we can control the electric and magnetic properties[30]. However, the existence of magnetism in MOFs has usually been ignored when it comes to magnetism. Magnetic ordering in moderate temperature requires a strong exchange interaction between magnetic atoms. However, MOFs' extended and porous nature makes this interaction small. One way of circumventing this issue is the use of a short linker[43]. Various magnetic properties were observed in MOFs with organic linkers with moderate size[44, 45, 46].

Among various 2D MOFs, MOFs in kagome lattice are expected to show exotic properties owing to their geometrically frustrated structure[47, 48]. In kagome MOFs, metal atoms from the kagome lattice and the organic linkers connect the metal atoms. Depending on the ligand positions, they can be called M_3L_2 or M_3L_1 type. Both experiments and theory suggest that they can host exotic properties such as 2D ferromagnetism, spin liquid, and QAHE[49, 50, 51, 52]. However, controlling magnetic properties in MOFs is usually a difficult task since large ligands usually result in the suppression of magnetic coupling between metal atoms, so the effect of ligands on magnetic properties must always be carefully examined from material to material. There also exist huge sets of ligands that can be inserted to connect metal atoms. We could adequately choose the ligand type depending on the target properties of interest. Thus, a general understanding of the critical factors determining the magnetic properties in kagome MOFs would enable us to utilize MOFs for further applications.

With this research being conducted on MOF systems, one critical question remains: Are the MOFs system suitable for studying 2D magnetism over magnetic vdW system? From the perspective of sample preparation, MOFs are expected to be good candidates for generating 2D nanosheets with high stability owing to their bottom-up synthesis and strong coordination bond[27, 26]. However, a magnetic system requires sophisticated exchange interaction between metal atoms. For the conventional transition metal oxides (TMOs) systems, the relation between electron filling and lattice geometry is relatively well-known [53, 54]. For instance, the half-filled system with 180° geometry between metal atoms leads to AFM coupling. However, since MOFs include various bonding characteristics differing from ligands to ligands, it is not certain whether this general picture established in the TMOs system still works. In TMOs, one usually treats the localized d electrons and considers their hybridization with neighboring p orbitals. However, whether this localized d picture would still be valid with complicated ligand molecular p orbitals in MOFs system is not certain. Thus, to extend the research on magnetism in MOF systems, we need to establish a basic understanding of the MOF system's electronic and magnetic structure.

In this thesis, we study the general magnetic properties of the 2D MOFs M_3L_2-the type where metal atoms M form kagome lattice and ligands L lie between metal triangles. Using first-principles density functional theory (DFT), we determine the magnetic ground states of various MOFs in M_3L_2 structure. We investigate the mechanism driving the magnetic ordering in these materials from the electronic structure calculations. We also examine magnetic anisotropy, an essential property of a 2D system. We find that magnetic ordering and anisotropy depend significantly on d electron occupation on the metal site. We also discuss the role of ligand types

and their effects on determining magnetic properties. Topological properties arising from the metal-ligand hybridization are also discussed. Throughout this analysis, we establish a general picture understanding of the electronic and magnetic properties in this kagome MOFs system.

This thesis is organized as follows:

In Chapter 2, the theoretical backgrounds for the technique used in the calculations are introduced. Density functional theory and related topics are briefly introduced. We also provide the computational details for our calculations.

In Chapter 3, we introduce the atomic structures used in our study. We show the structure properties and stability of the compounds.

In Chapter 4, we explain the electronic properties in kagome MOFs. The ligand field from square planar coordination plays an important role in determining electronic structure in kagome MOFs. We compare the electronic structures of various MOFs with magnetic configurations and show that energy level from square planar coordination is preserved. We also show the importance of ligand hole states.

In Chapter 5, we discuss the magnetic properties. We explain the microscopic origin of magnetic exchange and suggest which system becomes ferromagnetic and antiferromagnetic. Metal d_{zx}, d_{yz}, and ligand p_z state play a crucial role in determining the magnetic couplings. The effect of metal-ligand hybridization is also discussed. The relation between orbital occupation and magnetic anisotropy is also discussed.

In Chapter 6, we discuss the topological properties. We suggest MOFs with Fe and Mn could be a candidate for the realization of the Chern insulator at room temperature. We also propose the origin of this non-trivial band structure.

Chapter 7 concludes this thesis. We summarize our findings and provide a

perspective for future research.

Chapter 2

Computational Methods

This chapter introduces the background theories of the various calculation technique used throughout this thesis. We review the formalism of density functional theory (DFT), which is one method of calculating a given system's electronic structure. DFT+U methods enable us to correct the electron correlation effect underestimated in the LDA approach. Wannier function methods adopted in this study are briefly described.

2.1 Density Functional Theory

DFT is widely used to calculate the electronic structure of condensed matter systems because of their low computational cost compared to the all-electron calculation and their good transferability. The essence of DFT is that one can calculate the physical properties of a given system by calculating the electron density. Rather than solving the N-body Schrödinger equation and calculating the wavefunction, which is almost non-tractable, DFT tries to calculate the simple density function

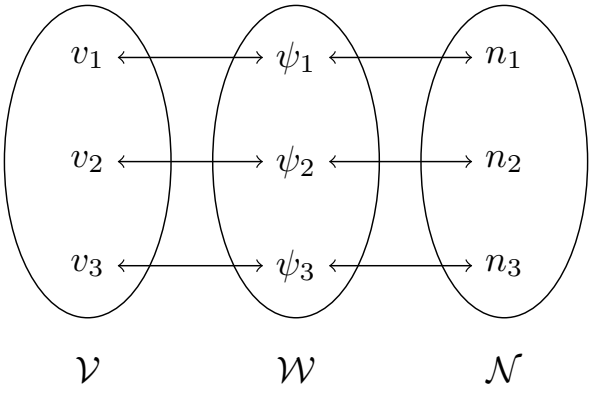

Fig. 2.1. One-to-one correspondence between external potentials v, ground state wavefnction ψ, and ground state densities n in the case of non-degenerate ground states.

and map this quantity to physical observables. There is mathematical proof that this mapping is exact, and in practical cases, we can use some approximation schemes to boost the computational times. The detailed theoretical backgrounds will be presented in the following sections.

2.2 Hohenberg-Kohn Theorem

The mathematical basis of the DFT is the bijective relation between Hamiltonian, wavefunction, and electron density. The computational cost makes it almost impossible to solve the N-body quantum mechanical problem by directly calculating the exact wavefunction. Instead, DFT tries to get the ground-state electron density $n(\mathbf{r})$, a scalar function of real space. The reason for calculating the ground state density is that a one-to-one correspondence exists between the ground state density, wavefunction, and the Hamiltonian. This relation is illustrated in the Fig. 2.1.

Let $\mathcal{V}, \mathcal{W}, \mathcal{N}$ be the set of external potentials v, ground state wavefunctions ψ, and the ground state electron density n. This figure means that there is a one-to-one correspondence between these sets. For example, if we fix the ground state density n_1, then there exist a unique external potential v_1 which gives the ground state wavefuction ψ_1 and the electron density n_1. We prove this relation in the case of non-degenerate ground states.

The injective relation of $\mathcal{V} \rightarrow \mathcal{W}$ is trivial due to the restriction to non-degenerate ground states. Its reverse map $\mathcal{W} \rightarrow \mathcal{V}$ is also injective. Assume that there exist some $|\psi_0\rangle$ which is ground state of two different potentials v_1 and $v_2 \neq v_1 + const.$ Then, $|\psi_0\rangle$ satisfies the Schrödinger equations,

$$\begin{aligned} \hat{H}|\psi_0\rangle &= [\hat{T} + \hat{v}_1 + \hat{W}]|\psi_0\rangle = E_1|\psi_0\rangle \\ \hat{H}|\psi_0\rangle &= [\hat{T} + \hat{v}_2 + \hat{W}]|\psi_0\rangle = E_2|\psi_0\rangle \end{aligned} \tag{2.1}$$

wherer $\hat{T}$ and $\hat{W}$ are the kinetic and interaction term respectively. Upon subtracting these two equation we get

$$[\hat{v}_1 - \hat{v}_2]|\psi_0\rangle = [E_1 - E_2]|\psi_0\rangle \tag{2.2}$$

If we write this relation in the real space basis, we get

$$\sum_{i=1}^{N} [v_1(\mathbf{r_i}) - v_2(\mathbf{r_i})] = E_1 - E_2 \tag{2.3}$$

for $\mathbf{r_i}$ for which ψ_0 does not vanish. Now, if we fix $N-1$ $\mathbf{r_i}$ and let the remaning coordinate to vary, Eq. 2.3 leads to a contradiction because we assumed that v_1 and v_2 differ by more than a constant. Thus, the mappig $\mathcal{W} \rightarrow \mathcal{V}$ is also injective and we get the bijective relation between $\mathcal{W}$ and $\mathcal{V}$.

We now turn to a map between $\mathcal{W}$ and $\mathcal{N}$. The mapping $\mathcal{W} \rightarrow \mathcal{N}$ is trivial because electron density n is defined as a square of the wavefunction ψ. Now, we

show the injective relation from $\mathcal{N}$ to $\mathcal{W}$. Assume that there exists some n_0 which can be obtained from the two different ground state wavefunction ψ_1 and ψ_2. From the variational principle, we obtain the inequality for the ground state energy E_1,

$$E_1 = \langle\psi_1|\hat{H}_1|\psi_1\rangle < \langle\psi_2|\hat{H}_1|\psi_2\rangle \tag{2.4}$$

By adding and subtracting v_2 to the right-hand side, we get

$$E_1 < E_2 + \langle\psi_2|\hat{v}_1 - \hat{v}_2|\psi_2\rangle \tag{2.5}$$

Since both wavefunctions yield same electron density n_0, this can be written as

$$E_1 < E_2 + \int d^3r n_0(\mathbf{r})[v_1(\mathbf{r}) - v_2(\mathbf{r})]. \tag{2.6}$$

But above argument can also be given with v_1 and v_2 quantities interchnaged,

$$E_2 < E_1 + \int d^3r n_0(\mathbf{r})[v_2(\mathbf{r}) - v_1(\mathbf{r})]. \tag{2.7}$$

Upon addition of these two inequalities, we end up with a contradiction,

$$E_1 + E_2 < E_2 + E_1. \tag{2.8}$$

Thus, we conclude that the mappig $\mathcal{N} \to \mathcal{W}$ is also injective and we again get the bijective relation between $\mathcal{W}$ and $\mathcal{N}$.

This result means that if we can identify the ground state density n, this quantity also uniquely determines the wavefunction: The ground state wavefunction is a density functional $\psi[n]$. Since all physical quantities can be obtained as an expectation value of wavefunction $\langle\psi|\hat{A}|\psi\rangle$, the one-to-one correspondence between wavefunction and density implies that these physical quantities are also density functional $A[n]$. Of course, the exact form of the density function is not known.

The above argument says that we can, in principle, map the density n, a relatively simple quantity to calculate, to the physical quantities. This theorem was suggested by Hohenberg and Kohn (HK) and formed the mathematical basis of the DFT formalism[55].

2.3 Kohn-Sham Approach

Even if the one-to-one correspondence between electron density and wavefunction provides the existence of the density functional $F[n]$, this theorem does not provide the exact form of the functional. One way of connecting this relation was provided by the Kohm-Sham (KS) scheme[56]. Before introducing KS scheme, we first consier a system of noninteracting electrons with a external potential V,

$$\hat{H} = \hat{T} + \hat{V} \tag{2.9}$$

Since this system is a noninteracting system, the corresponding N-particle ground state $|\Phi_0\rangle$ is a Slater determinant of a single particle states ϕ_i and the Schrödinger equations is written as

$$\left\{ -\frac{\hbar^2 \nabla^2}{2m} + v_s(\mathbf{r}) \right\} \phi_i(\mathbf{r}\sigma) = \epsilon_i \phi_i(\mathbf{r}\sigma). \tag{2.10}$$

The ground state density n_s and energy E_s corresponding to this noninteracting system is given by

$$\begin{aligned} n_s &= \sum_{\sigma} \sum_{i=1}^{N} |\psi_i(\mathbf{r}\sigma)|^2 \\ E_s &= \sum_{\sigma} \int d^3 r \phi_i^*(\mathbf{r}\sigma) \frac{(-i\hbar\nabla)^2}{2m} \phi_i(\mathbf{r}\sigma) + \int d^3 r v_s(\mathbf{r}) n_s(\mathbf{r}) \end{aligned} \tag{2.11}$$

At this point, one recollects that HK theorem is also valid for the noninteracting system. Then from Eq. 2.11, the ground state energy functional of noninteracting

system can be written as

$$E_s[n] = \langle \Phi[n] | \hat{T} + \hat{V} | \Phi[n] \rangle = \langle \Phi[n] | \hat{T} | \Phi[n] \rangle + \int d^3 r v_s(\mathbf{r}) n(\mathbf{r}) \tag{2.12}$$

Now, we return to the discussion of the interacting system. The KS approach assumes that an interacting system's ground state density n is simultaneously the ground state density of a noninteracting system with potential v_s. If such an auxiliary noninteracting system exists, we can utilize Eq. 2.12 to find the ground state density and its relation to the total energy. At this point, the strict proof that whether such an auxiliary system exists (*noninteracting v-representabily*) has not yet been proved. But it has been estabilished that we can find noninteracting v-representable density n arbitrarily close to the interacting system[57, 58, 59, 60]. Thus, we can follow the KS approach to treat interacting systems and solve noninteracting Hamiltonian for practical purposes.

Since the KS Hamiltonian should reflect the complex nature of the interacting system, the exact form of KS potential v_{KS} is also complex. One way of writing v_{KS} is to decompose the total energy $E[n]$ as

$$E[n] = T_s[n] + E_H[n] + E_{ext}[n] + E_{xc}[n]. \tag{2.13}$$

$T_s[n]$ is the single particle kinetic energy. $E_H[n]$ and $E_{ext}[n]$ is classical Hartree interaction energy and external potential term, respectively,

$$\begin{aligned} E_H[n] &= \frac{1}{2} \int d^3 r_1 \int d^3 r_2 n(\mathbf{r_1}) w(\mathbf{r_1}, \mathbf{r_2}) n(\mathbf{r_2}) \\ E_{ext}[n] &= \int d^3 r v_{ext}(\mathbf{r}) n(\mathbf{r}) \end{aligned} \tag{2.14}$$

$E_{xc}[n]$ is the exchange-correlation (XC) energy functional which absorbs all the complicated many-body effects of the interacting system. Then, the celebrated

Kohn-Sham equation from this energy decomposition can be written as,

$$\left\{-\frac{\hbar^2\nabla^2}{2m} + v_{ext}(\mathbf{r}) + v_H[n](\mathbf{r}) + v_{xc}[n](\mathbf{r})\right\}\psi_i(\mathbf{r}) = \epsilon_i\psi_i(\mathbf{r}) \tag{2.15}$$

The exact form of XC functional is not yet known. One approximation scheme is called local density approximation (LDA)

$$E_{xc-LDA}[n] = \int d^3r n(\mathbf{r})\epsilon_{xc-LDA}[n]. \tag{2.16}$$

In this scheme, the exchange-correlation energy $\epsilon_{xc-LDA}[n]$ is taken from the homogeneous electron system and is proportional to one-third of the electron density ($\epsilon_{xc-LDA}[n] \sim n^{\frac{1}{3}}$). By construction, LDA assumes slowly varying electron density and treats the inhomogeneous system as a piece-wise homogeneous system. Another improved scheme has also been suggested [generalized gradient approximation (GGA), meta-GGA. Finding good functional is still an important research area in the DFT community.

2.4 DFT+U Methods

One drawback of the LDA or GGA approach is its poor description of the strongly correlated system with d or f electrons. Since LDA itself assumes a homogeneous system, systems with strong electron-electron correlation could not be described by this universal form. This problem gets worse for the d electron system, and it has been reported that the LDA band gap underestimated the actual band gap of the system in general.

One way of solving this issue is adding an extra term in the KS Hamiltonian. Inspired by the Hubbard model, DFT+U (or LDA+U) formalism tries to add some extra terms to the total energy functional as

$$E_{LDA+U}[n] = E_{LDA}[n] + E^0_U[n] - E^0_{DC}[n]. \tag{2.17}$$

$E_{LDA}[n]$ is the original total energy functional in LDA scheme and $E_U^0[n]$ is the additional interaction term. $E_U^0[n]$ is given by the spherically averaged Coulomb energy U and exchange J as[61]

$$E_U^0[n] = \frac{1}{2}\sum_{\alpha} U_\alpha \sum_{i,j,\sigma} n_{\alpha,i}^{\sigma} n_{\alpha,j}^{-\sigma} + \frac{1}{2}\sum_{\alpha}(U_\alpha - J_\alpha) \sum_{i\neq j,\sigma} n_{\alpha,i}^{\sigma} n_{\alpha,j}^{\sigma} \tag{2.18}$$

In addition to this interaction term, we need to subtract the double counting term $E_{DC}^0[n]$ becasue some correlation terms were already included in the original LDA scheme. There exist many ways of choosing this double counting terms. If we choose the simplied form suggest by Han[61], the total LDA+U energy $E_{LDA}[n] = E_U^0[n] - E_{DC}^0[n]$ can be written as

$$E_{LDA}[n] = \frac{1}{2}\sum_{\alpha}(U_\alpha - J_\alpha) \sum_{\sigma} \{Tr(n_\alpha^\sigma) - Tr(n_\alpha^\sigma n_\alpha^\sigma)\}. \tag{2.19}$$

In this formalism, we do not need to modify the original DFT code because this additional term is calculated with the given density alone. It is important to choose a suitable range of U and J values to describe the interaction accurately. Although these parameters are manually selected fitting the DFT and experimental results, some suggested ways of calculating these parameters[62, 63].

2.5 Computational Details

We performed DFT calculations to determine the crystal and electronic structure of M_3L_2-type kagome MOFs. The OpenMX package based on the linear combination of pseudo-atomic orbital basis was used to perform DFT calculations[64]. Fully relativistic pseudopotentials were employed to determine the non-collinear magnetic ground state. The cutoff energy for real space integration was chosen to be 400 Ryd. The exchange-correlation effects were treated within the generalized gradient

approximation (GGA) level. For Brillouin zone integration, $9 \times 9 \times 1$ k-point mesh was used.

DFT+U_{eff} methods were also employed to treat the electron correlation effects of $3d$ states of transition metal atoms. However, the accuracy of DFT+U_{eff} methods depends on the choice of U_{eff} parameter. One way of determining this value is self-consistent calculation scheme treating U_{eff} as a linear response parameter[62]. For this calculation, we have employed the self-consistent determination of the U_{eff} scheme implemented in the Quantum-ESPRESSO (QE) package because of the absence of this feature in the OpenMX package[65, 62]. This scheme determined that the U_{eff} values ranged from 4 to 5 eV. These values are from the plane-wave basis package (QE), so we need to scale these values to corresponding values used in the atomic-orbital basis package (OpenMX). One possible approach is to match the band gap between two calculations. We adjusted U_{eff} values from OpenMX calculations to match the band gap from the QE calculation. In OpenMX, the corresponding U_{eff} values ranged from 2.5 to 4 eV. With this observation, we chose U_{eff} on metal site to be 3 eV for DFT+U_{eff} calculation in OpenMX.

We performed the Monte Carlo (MC) simulation to estimate the critical temperature T_c. The spins were treated as classical vectors, and the supercell size was chosen to be $40 \times 40 \times 1$. T_c was determined by analyzing the specific heat and magnetic susceptibility as a function of temperature.

Chapter 3

2D kagome MOFs

This chapter discusses the structure properties of 2D (M_3L_2). Different kinds of M_3L_2 can be realized by appropriate ligands. We calculate their monolayer structure properties, stability, and layer stacking issue.

3.1 Atomic Structure

The basic building blocks of MOFs are metal atoms and organic linkers. The organic ligands connect the metal atoms in this class of materials. In 2D kagome MOFs, the metal atoms from the kagome lattice and ligands sit between metal atoms.

Fig. 3.1 shows the simplied atomic structure of kagome lattice. In this figure, M represents the metal atom. To construct the kagome MOFs, we can connect these metal atoms by placing ligands L between the metal atoms. We have two possible spots for ligand placement when doing this: placing the ligand inside the empty hexagon (A) or the empty triangle (B). For the first case, the ligand occupies the empty hexagon, and the system becomes M_3L_1-type. In this case, the ligand is

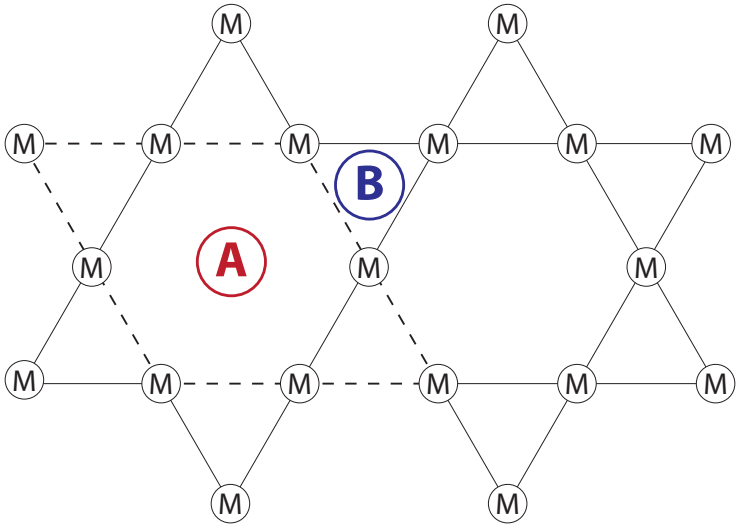

Fig. 3.1. Schematic crystal structure of kagome lattice. The unit cell is drawn with dashed lines. M represents metal atoms. A or B reprensents the possible position the ligands can be placed.

connected to six metal atoms. Interesting phenomena such as AFM kagome[51] or unconventional superconductivity[52] was reported in this system. For the second case, the ligand occupies the empty triangle site, and the system becomes M_3L_2 type. The major difference between these two cases is the symmetry and metal-metal distance. We have six-fold symmetry on the A site (M_3L_2 type) while three-fold symmetry exists on the B site. The metal-metal distance is also significantly affected by choice of ligand position. Even though we use the same ligand, the metal-metal distance becomes much longer for the M_3L_2 type because we need to enlarge the size of the empty triangle to accommodate the ligand. There can also exist structures by placing ligands on the positions of a mixture of A and B, but as far as our knowledge, no such structure is reported. In our study, we will focus on the second case.

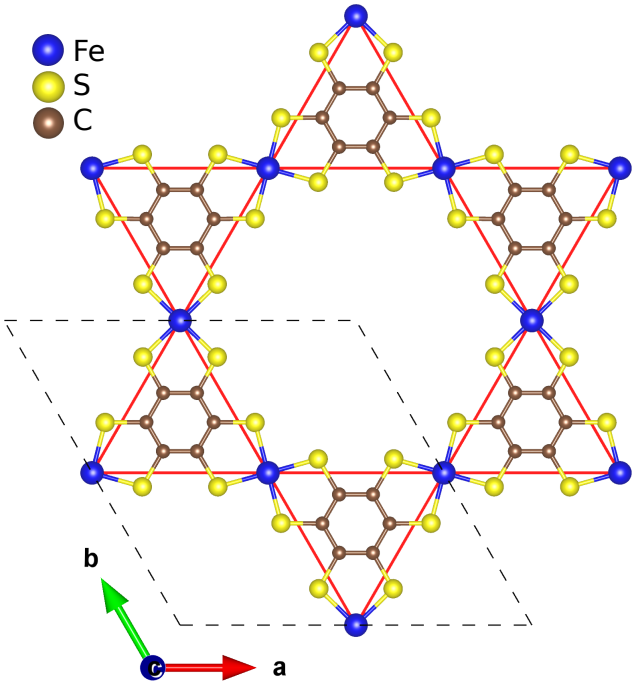

Fig. 3.2. Crystal structure of $Fe_3(C_6S_6)_2$. Fe (blue) atoms form a kagome lattice.

Fig. 3.2 shows the crystal structure of $Fe_3(C_6S_6)_2$, one of M_3L_2 type. We see that the metal atoms (Fe) form a kagome lattice, and the ligands (C_6S_6) are placed inside the empty triangle. Even with this small ligand, we see that the distance between metal atoms is far enough, so the direct interaction between metals would be very small. Thus, the metal-ligand hybridization plays a vital role in determining this system's structure and other properties.

In this thesis, we will focus on the 5 different types of ligands: C_6S_6, C_6O_6, C_6Se_6, HAB, and HITP. The crystal structures of three metal-bis-dithiolene complexes (C_6S_6, C_6O_6, C_6Se_6) are basically same as $Fe_3(C_6S_6)_2$ in Fig. 3.2. We can examine the effect of light and heavy halogen atoms by comparing the results with these ligands. MOFs with hexaaminobenzene HAB (HAB) show similar crystal

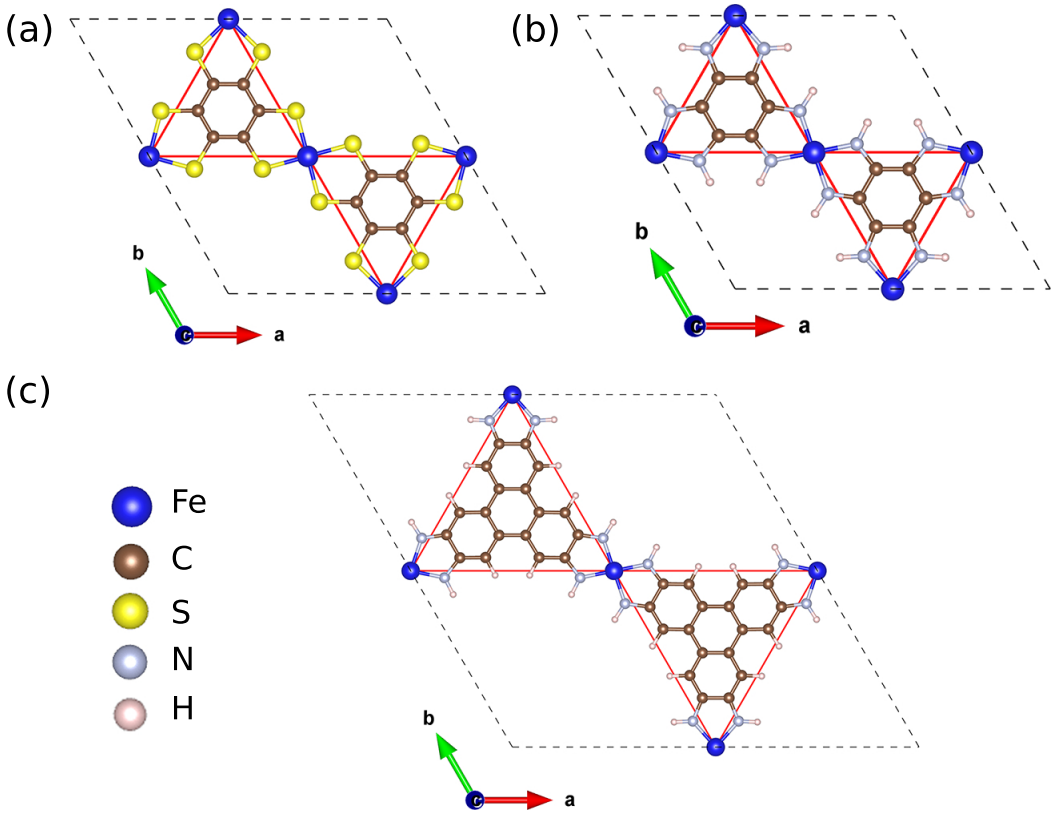

Fig. 3.3. Crystal structure of (a) $M_3(C_6S_6)_2$, (b) $M_3(HAB)_2$, and (c) $M_3(HITP)_2$ with Fe on metal site.

structure to bis-dithiolene case while the chalcogen atom is replaced to NH (Fig. 3.3(b)). Hydrogen is only connected to nitrogen, so the local structure near the metal atom is similar to the halogen case. MOFs with HITP contain hexaiminotriphenylene (HITP) on the ligand site (Fig. 3.3(c)). By comparing results with HAB and HITP, we can determine how the size and shape of ligands affect the electronic and magnetic structure. The representative crystal structure of each ligand is shown in Fig. 3.3.

Table 3.1 shows the calculated structure parameters of M_3L_2 system. Let us

Table 3.1: Structure properties of M_3L_2 system. Lattice constant (a) and distances between X and Y atoms (X-Y) are shown. M represnets the metal atom.

		Ti	V	Cr	Mn	Fe	Co	Cu
$M_3(C_6O_6)_2$	a(Å)	13.50	13.41	13.41	13.22	13.13	13.06	12.99
	M-M(Å)	6.75	6.71	6.71	6.61	6.57	6.53	6.50
	M-O(Å)	1.96	1.88	1.94	1.88	1.86	1.85	1.85
	O-O(Å)	2.99	3.02	2.90	2.95	2.95	2.92	2.92
$M_3(C_6S_6)_2$	a(Å)	15.39	15.23	15.11	15.00	14.84	14.73	14.67
	M-M(Å)	7.70	7.62	7.55	7.50	7.42	7.36	7.34
	M-S(Å)	2.35	2.29	2.28	2.27	2.19	2.16	2.16
	S-S(Å)	3.12	3.18	3.13	3.12	3.19	3.20	3.18
$M_3(C_6Se_6)_2$	a(Å)	16.00	15.88	15.75	15.67	15.51	15.40	15.34
	M-M(Å)	8.00	7.94	7.87	7.83	7.76	7.70	7.67
	M-Se(Å)	2.47	2.41	2.40	2.40	2.32	2.29	2.28
	Se-Se(Å)	3.22	3.27	3.25	3.22	3.30	3.31	3.29
$M_3(HAB)_2$	a(Å)	14.03	13.97	13.88	13.70	13.57	13.45	13.45
	M-M(Å)	7.02	6.98	6.94	6.85	6.78	6.72	6.70
	M-N(Å)	2.01	2.01	1.98	1.92	1.88	2.29	1.85
	N-N(Å)	3.05	3.03	3.03	3.07	3.09	3.31	3.08
$M_3(HITP)_2$	a(Å)	22.53	22.48	22.33	22.24	22.08	21.98	21.96
	M-M(Å)	11.27	11.24	11.17	11.12	11.04	10.99	10.98
	M-N(Å)	1.99	1.99	1.95	1.92	1.88	1.84	1.85
	N-N(Å)	7.34	7.32	7.34	7.35	7.37	7.38	7.36

first focus on $M_3(C_6O_6)_2$. We see that the lattice constant, metal-metal distance, and metal-halogen distance decrease from Ti to Ni due to the decreased atomic radius of transition metal atoms. However, the oxygen-oxygen distance does not vary significantly like other distances. The central carbon-carbon distance remains almost unchanged. This means that the structral properties inside the ligand remain almost the same regardless of the transition metal atoms.

For $M_3(C_6S_6)_2$ and $M_3(C_6Se_6)_2$, we see that lattice constant, metal-metal distance, and metal-halogen distance decrease from Ti to Ni. In contrast, halogen-halogen distances remain almost the same. Since the atomic radius of S and Se is larger than O, we see the overall distance increase. The average lattice constant for $M_3(C_6O_6)_2$ is about 13.1 Å. This value become about 15.1 Å for $M_3(C_6S_6)_2$, and 15.6 Å for $M_3(C_6Se_6)_2$. The ratio of the increase of lattice constant from $M_3(C_6O_6)_2$ to $M_3(C_6S_6)_2$ is about 15%, but it reduces to 3% for $M_3(C_6S_6)_2$ to $M_3(C_6Se_6)_2$ case. We also see that the bond length between metal and ligand increases significantly between $M_3(C_6O_6)_2$ and $M_3(C_6S_6)_2$. Since the electronic and magnetic properties depend on the hybridization between atoms, we expect that $M_3(C_6S_6)_2$ and $M_3(C_6Se_6)_2$ would show similar features.

Since $M_3(HAB)_2$ can be obtained by substituting S to NH, their structure parameters are almost the same. $M_3(HITP)_2$ shows the largest lattice constant because of its large ligand size. In this case, the metal-metal distance reaches about 11 Å, so the direct interaction between metal atoms almost vanishes. However, the local environment near the metal site remains almost the same as in the HAB case.

One thing to note is the difference between the M_3L_2 and M_3L_1 system. The ligands are placed inside the triangle in M_3L_2 while occupying the hexagon site in M_3L_1. Table 3.2 shows the difference in structral parameters in these two systems.

Table 3.2: Difference of structral parameters between $Fe_3(C_6O_6)_2$ and $Fe_3(CO)$.

	$Fe_3(C_6O_6)_2$	$Fe_3(CO)$
a(Å)	13.13	7.81
M-M(Å)	6.57	3.91
M-O(Å)	1.86	2.03
O-O(Å)	2.95	2.94

The lattice constant and metal-metal distance differs about twice. The Fe-Fe distance is 3.91 Å for the case of $Fe_3(CO)$, which is much shorter than $Fe_3(C_6O_6)_2$. This suggests that the direct interaction between metal atoms becomes more significant in the M_3L_1 system. On the other hand, the metal-oxygen distance slightly increases. For both cases, the oxygen-oxygen and carbon-carbon distance remain almost the same, implying the ligand bond does not significantly depend on the metal coordination. Thus, in the case of M_3L_2, the direct interaction between metal atoms would be much smaller, and the important exchange would always happen through the metal-ligand hybridization channel.

3.2 Planar Geometry

The five ligands in our study (C_6O_6, C_6S_6, C_6Se_6, HAB, and HITP) are basically planar ligands, which means that they reside on a single plane. However, depending on the coordinated metal species, this in-plane geometry can be modified from perfect in-plane to buckled geometry [66]. We compared the energy between these perfect in-plane and buckled cases and found that in-plane geometry is preferred for all cases. Similar results are also reported in various studies [67, 68].

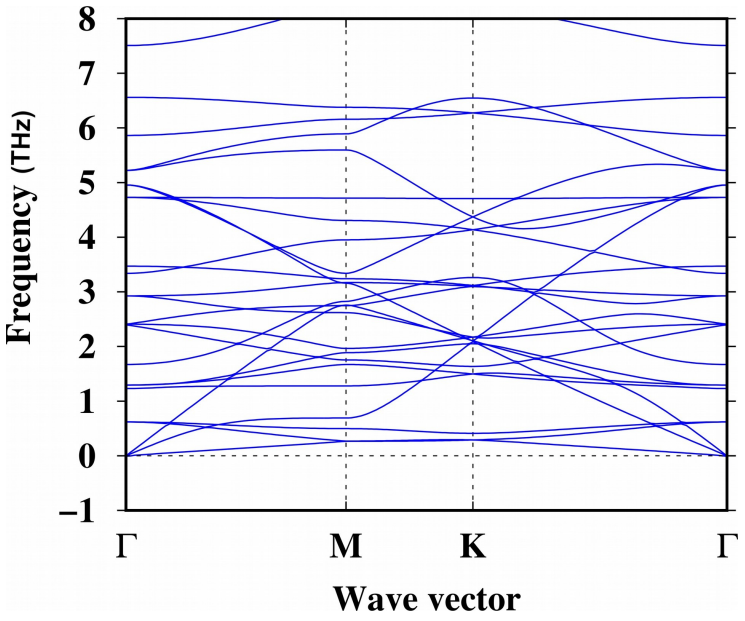

Fig. 3.4. Phonon dispersion of $Fe_3(C_6S_6)_2$ in square planar coordination.

To verify the stability of this planar structure, we employed phonon calculation on some selected compounds to be discussed in the later chapters. Fig. 3.4 shows the phonon dispersion relation calculated from planar structure. No imaginary frequency occurs on any mode, indicating that this structure is stable.

Chapter 4

Electronic properties

This chapter discusses the electronic structure of 2D kagome MOFs of M_3L_2-type. Different ligands and metals show different results, but the electronic structure arising from the square planar coordination around metal atoms exhibits some common behaviors. We first discuss the ligand hole states observed in the M_3L_2 system. In our calculation, these hole states are observed for all M_3L_2 systems and revealed to play an essential role in determining the magnetic interaction, which will be discussed in a later chapter. We then show how the effect of ligand field changes on various ligands and magnetic configurations.

4.1 Oxidation states

When discussing the electronic properties of transition metals, their oxidation state plays an important role. Naively, we may estimate the metal would be M^{4+} state because HAB ($C_6H_6N_{12}$), for instance, loses six hydrogens during the reaction process, thus being $[C_6H_6N_6]^{6-}$ state. As reported in various studies[69, 34, 70, 31],

however, the formal charge on the metal site is known to be M^{2+}, or a mixture of M^{1+} and M^{3+}. This happens because the reaction process includes both the oxidation and deprotonation processes. For example, Feng *et al*. reports that the synthesis of HAB-Cu and Ni requires both oxidation and deprotonation steps [71]. During the deprotonation process, HAB is exposed to the basic condition and loses three hydrogen atoms. Then, this sample suffers an oxidation reaction with oxygen, thus resulting in the HAB3− state. Both steps are required in the synthesis process, and they report that the oxidation state of metal atoms is observed to be M^{2+}.

Table 4.1: Bader charge analysis of $M_3(C_6O_6)_2$, $M_3(C_6S_6)_2$, and $M_3(C_6Se_6)_2$.

	Ti	V	Cr	Mn	Fe	Co	Ni
$M_3(C_6O_6)_2$ (U_{eff}=0 eV)	1.94	1.75	1.40	1.60	1.40	1.17	1.01
$M_3(C_6O_6)_2$ (U_{eff}=3 eV)	1.86	1.68	1.44	1.54	1.34	1.11	1.05
$M_3(C_6S_6)_2$ (U_{eff}=0 eV)	1.64	1.27	1.07	1.12	0.86	0.63	0.43
$M_3(C_6S_6)_2$ (U_{eff}=3 eV)	1.57	1.34	1.12	1.06	0.82	0.60	0.51
$M_3(C_6Se_6)_2$ (U_{eff}=0 eV)	1.52	1.14	0.97	0.97	0.68	0.46	0.25
$M_3(C_6Se_6)_2$ (U_{eff}=3 eV)	1.22	1.19	0.99	0.92	0.63	0.41	0.30

To verify the oxidation states, we performed the Bader charge analysis. Table 4.1 shows the calculated Bader charges for given system. Both U_{eff}=0 and 3 eV calculations are shown. We see that the Bader charge decreases as the ligand gets heavier. For instance, we see the Bader charge of Mn decreases from 1.60 $\rightarrow$ 1.12 $\rightarrow$ 0.97 for U_{eff}=0 eV calculation. As the atomic number increases, the covalent character increases, and the electronegativity decreases. Comparing these Bader charge results to the other well-known systems, we find that the metal oxidation number becomes M^{2+} state [72, 73].

4.2 Ligand Field in Square Planar Coordination

The metal sites in these M_3L_2-type MOFs have a local structure of four neighboring atoms in a planar configuration regardless of the type of ligand molecules. For example, the Fe atom in $Fe_3(C_6S_6)_2$ (Fig. 3.3(a)) is surrounded by four sulfur atoms. Also, other 2D MOFs with various ligands are reported to exhibit the same four-fold planar coordination [74, 75, 76]. The local environment of a metal atom in M_3L_2-type MOFs is not necessarily square planar, but, in practice, the magnitude of rectangular distortion is negligible for most cases. Since the energy level splitting between d_{yz} and d_{zx} orbitals is minimal compared to their bonding or bandwidth, for the sake of simplicity, we assume the square planar field for the rest of the discussion. The common local structure, i.e., square planar coordination of metal atoms, indicates the same basis of metal-ligand interactions regardless of the type of ligands. Thus, we expect to see a common feature in the basic electronic structure of the M_3L_2 system near the Fermi level arising from the partially filled d-electrons of metal atoms under the ligand field of the square planar coordination.

In M_3L_2-type MOFs, the transition metal atoms form a kagome lattice. The detailed structural or electronic properties depend on the metal atoms' ligands. The local environment of a metal atom also depends on the ligand type, which determines the ligand field splitting on the metal site. However, as we verified from Fig. 3.3, the local environment around the metal site in M_3L_2-type MOFs looks similar. For metal-bis-dithiolene complexes ($M_3(C_6O_6)_2$, $M_3(C_6S_6)_2$, $M_3(C_6Se_6)_2$), the metal atom is surrounded by four chalcogen atoms in square shape. There exists a slight distortion from square to rectangle, but the distortion is small. For HAB or HITP, the metal atom is also surrounded by four nigtoren atoms. In this case, we have additional hydrogen atoms attached to nitrogen, so their overlap with metal

is small. So, we can say that the local environment around the metal site is square planar coordination in M_3L_2-type MOFs regardless of the ligand type. Since the ligand field arising from this specific coordination induces unique energy splitting of metal d orbitals, understanding the general energy splitting of the square ligand field enables us to easily analyze the electronic and magnetic properties of these MOFs systems.

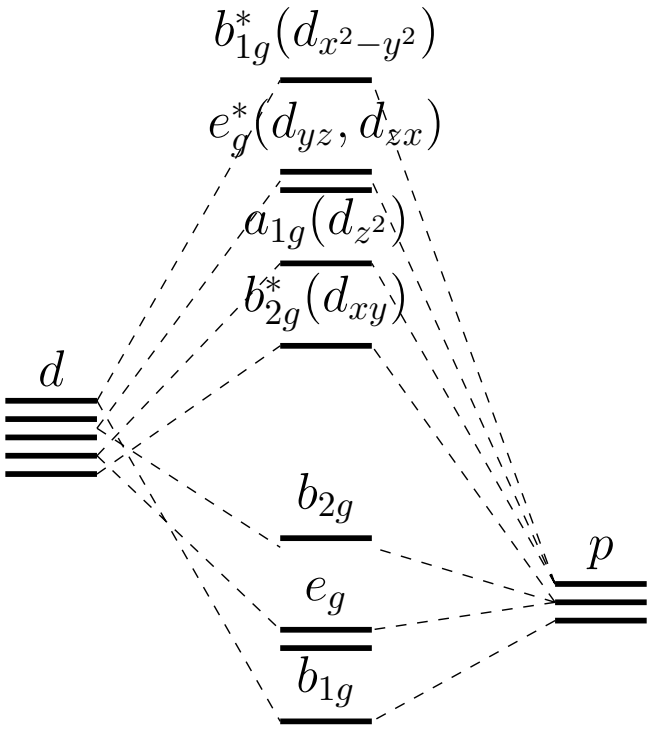

Fig. 4.1. Ligand field splitting of d orbitals in square planar coordination.

As a first step, we discuss the isolated d orbitals in square-planar coordination. Fig. 4.1 shows the general ligand field splitting of d orbitals in square planar coordination. We assume the orbital energy of d level lies above p orbitals. In this case,

the major components of antibonding orbitals are d orbitals. By symmetry, five d orbitals are categorized into four-manifolds. The covalent nature of σ bonding in b_{1g} ($d_{x^2-y^2}$) is strong, while the hybridization between a_{1g} (d_{z^2}) and p_z orbitals are negligible. The b_{2g} (d_{xy}) and e_g (d_{zx}, d_{yz}) states also carry a relatively strong $dp\pi$-hybridization, leading to a large bandwidth with a relatively small crystal field effect.

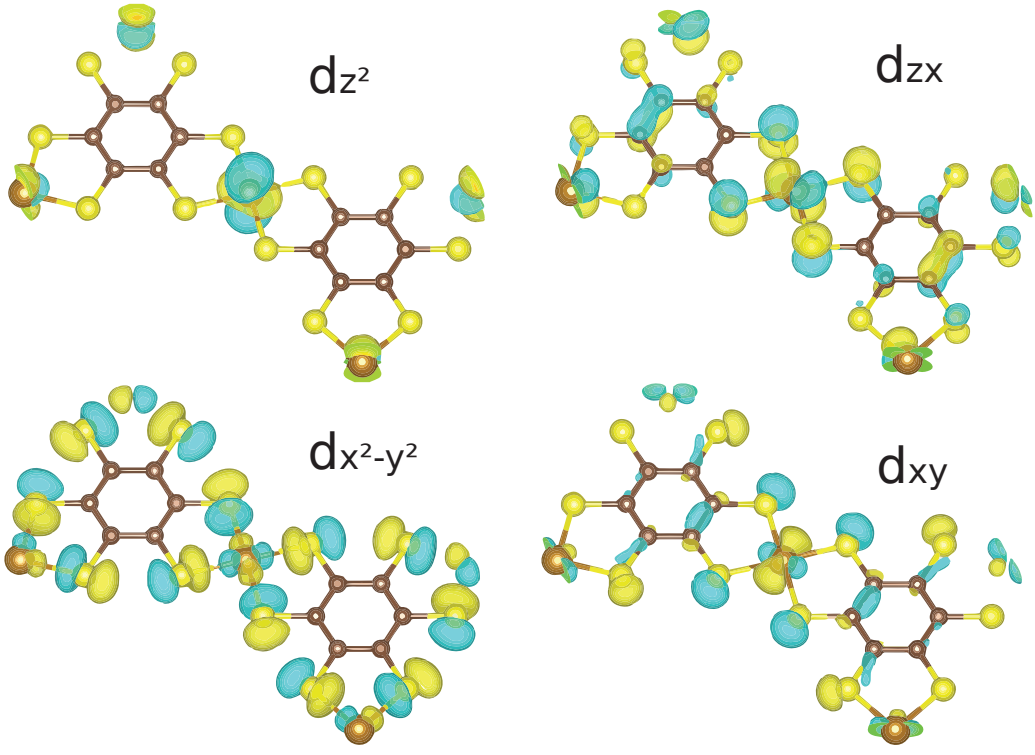

Fig. 4.2. Various wavefunctions of different energy levels calculated at Γ point in $Mn_3(C_6S_6)_2$.

The feature of ligand field splitting can further be verified by examining the wavefunction character. Fig. 4.2 shows the real space wavefunction of d orbitlas. We can see that d_{z^2} contains almost no p component, which verifies the nonbonding

character of a_{1g} state. d_{zx} shows moderate $dp\pi$-bonding character, while b_{1g} shows the strongest $dp\sigma$-hybridization, which implies they form a strong covalent bonding. d_{xy} also shows $dp\pi$-bonding as d_{zx}, but the magnitude of p orbitals is relatively small compared to d_{zx} case.

Here, one should note that the energy diagram of d orbitals in 2D kagome MOFs is slightly different from the perfect square planar complexes. The angular overlap model, for instance, suggests the energy of d orbital in square planar coordination becomes

$$E(d_{xy}) = 4V_{\pi}^{'} \tag{4.1}$$

$$E(d_{yz}) = E(d_{zx}) = 2V_{\pi} \tag{4.2}$$

$$E(d_{x^2-y^2}) = 3V_{\sigma} \tag{4.3}$$

$$E(d_{z^2}) = V_{\sigma} - 4V_{ds}. \tag{4.4}$$

For a square planar system with D_{4h} symmetry such as $[PdCl_4]^{2-}$, we usually have $V_{\pi}^{'} = V_{\pi}$. This means that $E(d_{xy})$ should lie above $E(d_{yz}) = E(d_{zx})$ for the π-donor system as this case. However, the situation is different in the M_3L_2 system. In $Fe_3(C_6S_6)_2$, for instance, the local symmetry around metal is actually D_{2h}. The strong sp^2 bonding between C and S lowers the energy of the in-plane σ-bonding p orbital of S. This effectively lowers the energy of that p ligand orbital. This weakens the $dp\pi$-hybridization between that p-ligand orbital and metal-d_{xy}. Thus, the effecitve in-plane $dp\pi$ hybridization energy ($\tilde{V}_{\pi}^{'}$) becomes very small, and the energy of e_g level lies above it. There also exists a splitting between e_g states, but their splitting is usually small compared to their bandwidth in an extended system.

Another issue is that a small distortion of ligand coordination exists in a real system from square to rectangle geometry. The distortion from square to rectangu-

lar field only causes small energy spitting between the two degenerate d_{yz} and d_{zx} energy levels. This effect can be ignored considering the bandwidth of each level in an extended system. In our calculation, this distortion was even small enough to induce a significant energy difference from the square planar ligand picture.

Thus, it remains a question whether the simple picture of Fig. 4.1 can explain all the features of electronic band structures for extended systems like the 2D M_3L_2 Kagome MOFs. For instance, the magnitude of $p-d$ hybridization varies depending on neighboring atoms, e.g., N or chalcogen atoms. When magnetic ordering is present, the degree of magnetic exchange interactions affects the order of each ligand field level. The structural distortion mentioned above also could matter. Despite the significant variations in the split levels, we find a surprisingly common ground for the states near the Fermi level for all the M and L elements cases in the M_3L_2 systems. To get an insight into the critical parts of the M_3L_2 electronic band structures, let us examine energy level diagrams of three typical cases: $Ti_3(C_6S_6)_2$, $Cr_3(C_6S_6)_2$, and $Fe_3(C_6S_6)_2$.

4.2.1 $Ti_3(C_6S_6)_2$ Nonmagnetic insulator

The ground state of $Ti_3(C_6S_6)_2$ is a nonmagnetic (NM) insulator. The projected density-of-states (PDOS) shown in Fig. 4.3 are pretty consistent with the simple ligand field picture for the square planar coordination as illustrated in Fig. 4.1. The bonding-antibonding states of the b_{1g} state span from -4 eV below the Fermi level to 4 eV above. Due to the strong $dp\sigma$ hybridization, the b_{1g} bonding state has a covalent character. Narrow a_{1g} and b_{2g} bands above the Fermi level exhibit non-bonding and weak hybridization characteristics, respectively. The e_g bands represent the bonding and antibonding state, separated by about 2 eV. The band-

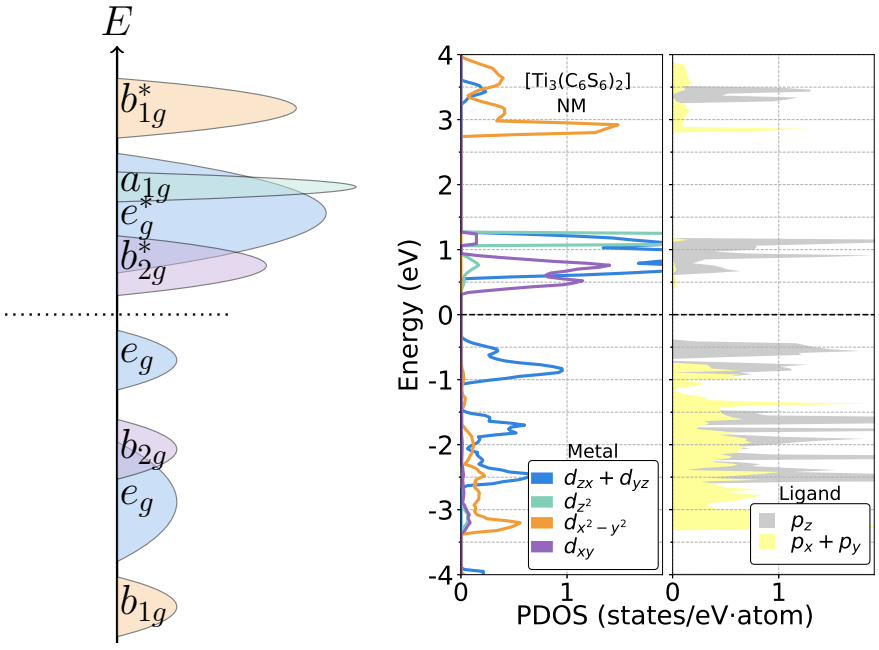

Fig. 4.3. PDOS of $Ti_3(C_6S_6)_2$ in nonmagnetic configuration. PDOS of Metal d levels and ligand p levels are shown.

width of the e_g bands reflects the strength of $dp\pi$ hybridizations of d_{zx} and d_{yz} orbitals, as illustrated in Fig. 4.3.

The bandgap is formed by the unoccupied b_{2g}^* and occupied e_g^* bands. The unoccupied e_g^* bands are heavily hybridized with S p_z orbitals, leaving *effectively* two holes in the ligand. Hence, the electron configuration of $Ti_3(C_6S_6)_2$ is close to $d^2\underline{L}^2$, where d^2 corresponds to the occupied e_g states. We will discuss the electron configuration in detail later in this section.

Another feature is the weak hybridization of the b_{2g} level. The pure square planar geometry puts equal footing on hybridizing the in-plane and out-of-plane $dp\pi$. However, as discussed in the Sec. 4.2, the local ligand coordination effectively

suppresses the in-plane $dp\pi$ hybridization. This is observed in the band structure. Between energy 0 and 1 eV, we see there exist three states, a_{1g}, e_g^*, and b_{2g}^*. As in the ideal square planar ligand field, a_{1g} remains almost nonbonding orbital. The e_g sate shows sizable hybridization between d_{yz}-d_{zx} and p_z orbitals. However, we observe d_{xy} shows almost no hybirdization with p_x and p_y orbitals. As discussed in the Sec. 4.2, the in-plane $dp\pi$ hybridization becomes very weak due to the ligand coordination, which induces almost ionic rather than covalent bonding even with $dp\pi$ hybridization.

4.2.2 $Cr_3(C_6S_6)_2$ Non-collinear AFM metal

The ground state of $Cr_3(C_6S_6)_2$ is a non-collinear AFM metal. In the majority spin (spin-↑) channel, for example, the strong exchange interaction pushes down the localized $a_{1g}^{\uparrow}$ and $b_{2g}^{*\uparrow}$ level well below the Fermi level, as shown in Fig. 4.4. Also, the $e_g^{*\uparrow}$ $dp\pi$-bands, consisting of mostly Cr d_{zx} and d_{yz} orbitals, are almost fully occupied, leaving a small gap with the unoccupied $dp\pi$-antibonding bands consisting of S p_z states in the same spin-↑ channel. Thus, the local magnetic moment of Cr is close to 4 μ_B corresponding to d^4. On the contrary, Cr's minority spin (spin-↓) channel is almost empty, and the Cr d spin-↓ orbitals are pushed up well above the Fermi level. Consequently, the S p_z states hybridized with the neighboring Cr e_g states of both spins form a band crossing the Fermi level so that the system becomes metallic. Therefore, the energy level order within each spin channel is consistent with the simple ligand field splitting of Fig. 4.1. Despite the strong local moment of Cr, the covalent nature of b_{1g} bonding is still robust, and the b_{1g} contribution to the magnetic moment of Cr is negligible.

The ground state of $V_3(C_6S_6)_2$ is also a non-collinear AFM metal with a similar

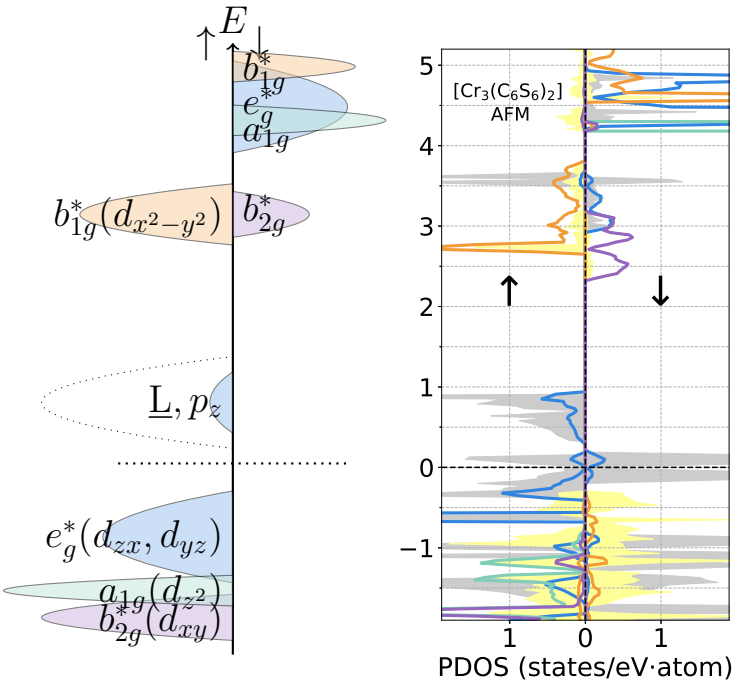

Fig. 4.4. Spin-resolved PDOS of $Cr_3(C_6S_6)_2$ in antiferromagnetic ground state. PDOS of Metal d levels and ligand p levels are shown. Data on left (right) represents the PDOS of spin-up (spin-down) channel.

electronic structure except that one less d electron is missing from the a_{1g} state, i.e., corresponding to the d^3 configuration.

4.2.3 $Fe_3(C_6S_6)_2$ FM half-metal

The ground state of $Fe_3(C_6S_6)_2$ is an FM half-metal. As shown in Fig. 4.5, the ordering of ligand field levels in each spin channel is quite consistent with that of the simple picture of Fig. 4.1. In the majority spin (spin-↑) channel, all the localized d

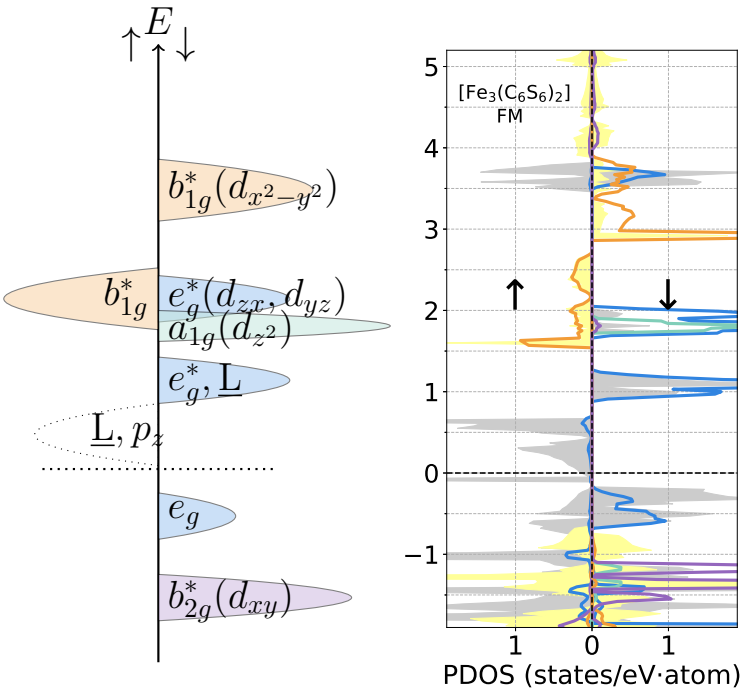

Fig. 4.5. Spin-resolved PDOS of $Fe_3(C_6S_6)_2$ in ferromagnetic ground state. PDOS of Metal d levels and ligand p levels are shown. Data on left (right) represents the PDOS of spin-up (spin-down) channel.

orbital states except the antibonding b^*_{1g} level are fully occupied. Remarkably, the covalent nature of b_{1g} is robust, despite the large on-site magnetic moment. The b_{1g} occupation is close to one reflecting its covalent character, but the b_{1g} state is slightly spin-polarized due to the FM ordering. In the minority spin (spin-↓) channel, only the localized b^*_{2g} level is fully occupied. On the other hand, an interesting contribution to the states near the Fermi level comes from the $e^{*\downarrow}_g$ bands. Although the a_{1g} level is supposed to be below the e^*_g level in the simple picture of Fig.

4.1, the $dp\pi$-hybridized e_g bands lie below and above the Fermi level, respectively. Contrary to the finite bandgap in the spin-$\downarrow$ channel, the ligand S $p_z^{\uparrow}$ band in the spin-$\uparrow$ channel slightly hybridized with the $e_g^{*\uparrow}$ states touches the Fermi level and makes this $Fe_3(C_6S_6)_2$ a half-metal.

One of the primary aspects of the electronic structure of FM M_3L_2 systems is the presence of the e_g and e_g^* bands across the Fermi level in the spin-$\downarrow$ channel. While the local moment at the metal site arises from the localized orbitals like a_{1g} and b_{2g} states in both spin channels, the e_g^* states with relatively strong $dp\pi$-hybridization form bands and play a crucial role in determining the effective exchange interactions between the neighboring metal sites.

4.2.4 Common features

Fig. 4.6 illustrates a summary of the d-electron occupations in each ligand field manifold for the series of M_3L_2 systems as obtained from the DFT+U calculations with U_{eff}=3 eV. First, the b_{1g} occupations remain close to one for all the $3d$ transition metal elements from Ti to Ni, demonstrating the strong covalency of $dp\sigma$-hybridization between M and S. Second, the step-wise changes of the b_{2g} and a_{1g} occupations reflect the localized character of the b_{2g} and a_{1g} orbitals. Finally, the variations of the e_g^* occupation exhibit different features in the AFM and FM ranges, respectively. For instance, the $e_g^{*\uparrow}$ orbitals are partially occupied with almost empty $e_g^{*\downarrow}$ states in the AFM range of V and Cr, while the $e_g^{*\uparrow}$ orbitals are fully occupied for the FM cases of Mn, Fe, and Co. Further, we observe a systematic increase of the $e_g^{\downarrow}$ band occupation along M = Mn, Fe, and Co in the FM range. Here, the $e_g^{*\uparrow}$ occupation numbers listed in Fig. 4.6 remain the same regardless of the choice of U_{eff} parameters. However, the $e_g^{\downarrow}$ band occupations are easily affected

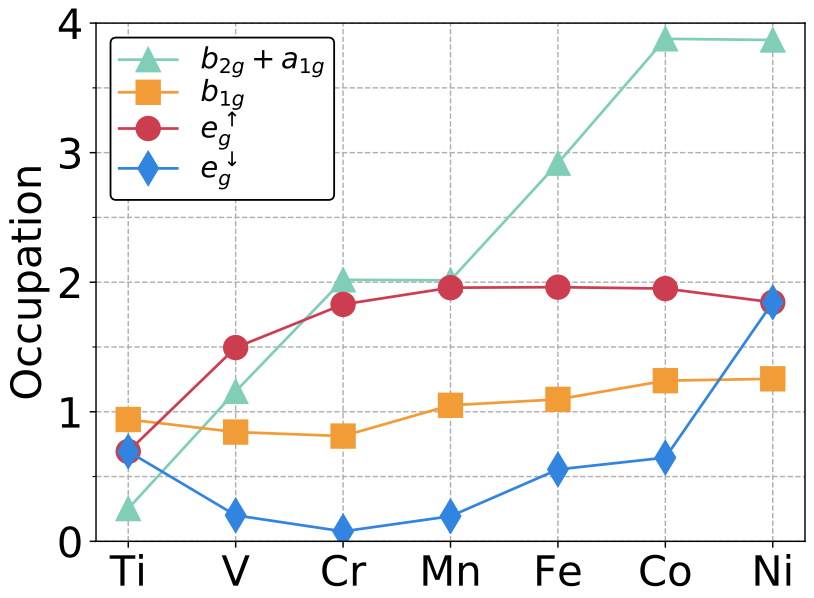

Fig. 4.6. Occupation number of each d orbital of $M_3(C_6S_6)_2$ system with U_{eff}=3 eV calculations. The d occupations in both bonding and antibonding states are summed up.

by choice of U_{eff} because of their partial occupation and bands lying across the Fermi level. Since the e_g level position relative to the Fermi level is important to the effective magnetic interactions, its dependence on the d-electron occupation is crucial to understanding the effective exchange interactions and magnetic ordering temperatures. We will discuss this issue in the next section.

Chapter 5

Magnetic properties

This chapter discusses the magnetic properties of the M_3L_2-type kagome MOFs. The electronic structure calculations verified that the energy structure of d levels from the square planar ligand field is well preserved regardless of ligand type. Since magnetism usually comes from d electrons, we can expect that magnetic structure would also show common behavior regardless of ligand type. This actually turns out to be true, and the occupation of the d level is an essential factor for determining magnetic interaction in M_3L_2-type MOFs.

We examine the magnetic ground states, their deriving mechanism, magnetic anisotropy, and some interlayer effects. Our calculations reveal general trends in the magnetic ordering regardless of the ligand type. The transition metal type is the key factor determining the magnetic properties, especially its d electron occupation. Among d levels, the occupation on e_g level plays a crucial role in determining the magnetic ground state. We also study how magnetic anisotropy can be determined by considering d orbital occupation.

5.1 Magnetic Ground States

Table 5.1 shows the magnetic ground states of M_3L_2 systems for the series of $3d$ transition metal atoms (M = Ti, V, Cr, Mn, Fe, Co, and Ni) and various ligands (L = C_6O_6, C_6S_6, C_6Se_6, HAB, and HITP), as determined from DFT+U calculations with U_{eff}= 0 and 3 eV. The group of transition metals separates the NM, AFM, and FM phases. In other words, the magnetic ordering depends on the metal M, i.e., the local electronic structure at the $3d$ transition metal site. The Ti- and Ni-M_3L_2 are NM. The V- and Cr-M_3L_2 systems are AFM. However, the complex character of non-collinear ordering labeled as AFM_A and AFM_E depends on the type of the ligand (See Fig. 5.2 for more information on the detailed spin configurations.). The Mn-, Fe-, and Co-M_3L_2 systems are FM except for the case of $Co_3(C_6O_6)_2$ from the U_{eff}=0 eV calculation and the case of $Mn_3(C_6Se_6)_2$ from the U_{eff}=3 eV calculation. We will discuss the role of U_{eff} in detail later. The role of ligands, i.e., metal-ligand hybridization, is not critical but significant. We identify the magnetic anisotropy among the FM-ordered states: Mn and Fe favor the out-of-plane direction ($FM_\perp$) except for the $Fe_3(C_6O_6)_2$ case. The rest of Co-M_3L_2 systems favor in-plane FM ($FM_\parallel$).

Calculated total energies for different spin configurations with different U_{eff} values are shown in Fig. 5.1 for the series of M = V, Cr, Mn, Fe, and Co with L = C_6O_6, C_6S_6, and C_6Se_6. The plots demonstrate clearly that V and Cr systems favor AFM ordering contrary to the FM ground states of Mn, Fe, and Co. Overall, the energy difference between FM and AFM is an order of 100 meV, whereas the difference between $FM_\parallel$ and $FM_\perp$ is indistinguishable in the scale of the drawing. Further, the ground state spin configurations are independent of the choice of U_{eff} values, i.e., U_{eff}= 0 and 3 eV. Still, we observe a significant effect of U_{eff} on the

Table 5.1: Magnetic ground states of M_3L_2 systems obtained from DFT+U calculations with U_{eff}= 0 and 3 eV. When the ground states for different U_{eff} values do not match each other, the U_{eff}=3 eV result is shown in parentheses. $d^n\underline{L}^m$ represents the number of metal d electrons and ligand p holes. The spin configuration for each magnetic ordering is displayed in Fig. 5.2.

	Ti	V	Cr	Mn	Fe	Co	Ni
	$d^2\underline{L}^2$	$d^3\underline{L}^2$	$d^4\underline{L}^2$	$d^5\underline{L}^2$	$d^6\underline{L}^2$	$d^7\underline{L}^2$	$d^8\underline{L}^2$
C_6O_6	NM	AFM_A	AFM_A	$FM_\perp$	$FM_\parallel$	$AFM_A(FM_\parallel)$	NM
C_6S_6	NM	AFM_A	AFM_A	$FM_\perp$	$FM_\perp$	$FM_\parallel$	NM
C_6Se_6	NM	AFM_E	AFM_E	$FM_\perp(AFM_E)$	$FM_\perp$	$FM_\parallel$	NM
HAB	NM	AFM_E	AFM_A	$FM_\perp$	$FM_\perp$	$FM_\parallel$	NM
HITP	NM	AFM_A	AFM_A	$FM_\perp$	$FM_\perp$	$FM_\parallel$	NM

AFM-FM energy difference for V-M_3L_2 systems. We also note that the energy difference between AFM_A and AFM_E is far smaller than AFM-FM orderings. Although the lowest energy of $Co_3(C_6O_6)_2$ turns out to be AFM_A, the total energies of all the FM and AFM configurations are nearly degenerate, implying that the effective exchange interactions are negligible.

In the case of an FM system, it is also important to identify the magnetic properties of the ground state. Table 5.2 and 5.3 show the ground state properties of each FM system. Each system belongs to one of metal (M), half-metal (HM), magnetic semiconductor (MS), bipolar magnetic semiconductor (BMS), and insulator (I) systems. The properties heavily depend on the U_{eff} values used in the calculations. The U_{eff}=0 eV calculations show M, HM, and BMS behaviors. We see that systems with heavy ligands, for instance, HITP, show the insulating property while light

Table 5.2: Ground state and energy parameters from U_{eff}=0 eV calculations. Each symbol in the type represent Metal (M), Half-metal (HM), magnetic semiconductor (MS), bipolar magnetic semiconductor (BMS), and insulator (I). $\Delta_{\uparrow}$ and $\Delta_{\downarrow}$ represent the energy difference between CBM and VBM of spin-up and spin-down channel. For HM and BMS, Δ_{sf}, Δ_2, and Δ_3 represent band gap, spin-flip energy in valence band, and spin-flip energy in conduction band, respectively.

	Type	$\Delta_{\uparrow}$	$\Delta_{\downarrow}$	Δ_{sf}	Δ_2	Δ_3
$Mn_3(C_6O_6)_2$	HM	0	0.96	0.66		
$Fe_3(C_6O_6)_2$	HM	0	0.49	0.31		
$Co_3(C_6O_6)_2$	M	0	0			
$Mn_3(HAB)_2$	HM	0	0.35	0.15		
$Fe_3(HAB)_2$	HM	0	0.13	0.03		
$Co_3(HAB)_2$	M	0	0			
$Mn_3(C_6S_6)_2$	HM	0	0.69	0.54		
$Fe_3(C_6S_6)_2$	MS	0.06	0.71			
$Co_3(C_6S_6)_2$	BMS			0.14	0.05	0.12
$Mn_3(C_6Se_6)_2$	MS	0.04	0.74			
$Fe_3(C_6Se_6)_2$	MS	0.12	0.80			
$Co_3(C_6Se_6)_2$	BMS			0.08	0.15	0.38
$Mn_3(HITP)_2$	MS	0.09	0.68			
$Fe_3(HITP)_2$	MS	0.14	0.51			
$Co_3(HITP)_2$	I	0.24	0.31			

Table 5.3: Ground state and energy parameters from U_{eff}=3 eV calculations. Each symbol in the type represent Metal (M), Half-metal (HM), magnetic semiconductor (MS), bipolar magnetic semiconductor (BMS), and insulator (I). $\Delta_{\uparrow}$ and $\Delta_{\downarrow}$ represent the energy difference between CBM and VBM of spin-up and spin-down channel. For HM and BMS, Δ_{sf}, Δ_2, and Δ_3 represent band gap, spin-flip energy in valence band, and spin-flip energy in conduction band, respectively.

	Type	$\Delta_{\uparrow}$	$\Delta_{\downarrow}$	Δ_{sf}	Δ_2	Δ_3
$Mn_3(C_6O_6)_2$	HM	0	1.71	1.36		
$Fe_3(C_6O_6)_2$	HM	0	0.41	0.23		
$Co_3(C_6O_6)_2$	M	0	0			
$Mn_3(HAB)_2$	HM	0	1.40	1.18		
$Fe_3(HAB)_2$	HM	0	0.51	0.41		
$Co_3(HAB)_2$	M	0	0			
$Mn_3(C_6S_6)_2$	HM	0	1.47	1.43		
$Fe_3(C_6S_6)_2$	HM	0	1.20	1.07		
$Co_3(C_6S_6)_2$	HM	0	1.00	0.88		
$Mn_3(C_6Se_6)_2$	HM	0	1.42	1.38		
$Fe_3(C_6Se_6)_2$	HM	0	1.25	1.12		
$Co_3(C_6Se_6)_2$	HM	0	1.19	1.05		
$Mn_3(HITP)_2$	HM	0	1.80	1.65		
$Fe_3(HITP)_2$	HM	0	0.83	0.75		
$Co_3(HITP)_2$	MS	0.08	0.64			

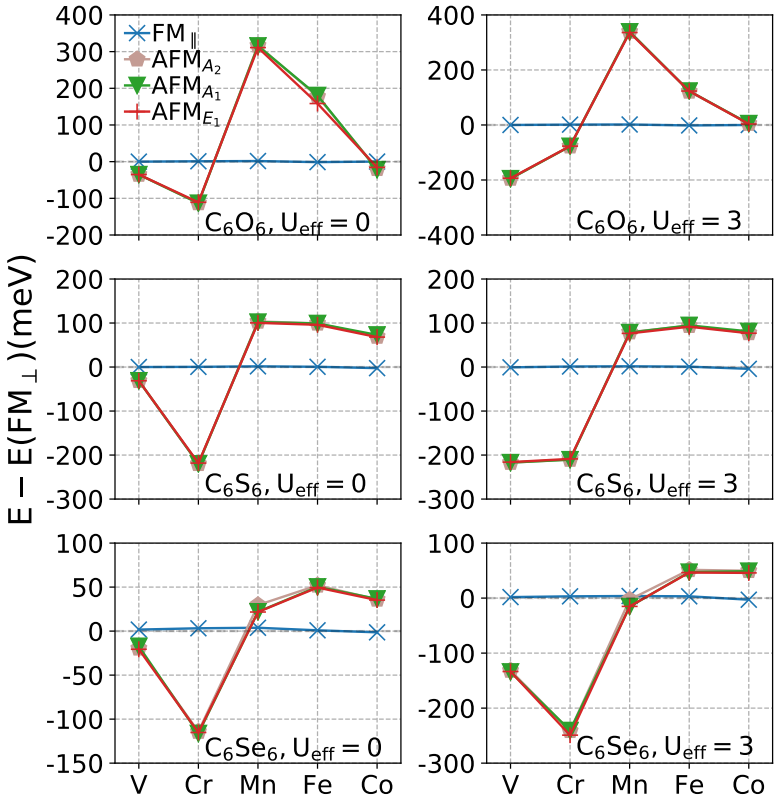

Fig. 5.1. DFT+U total energies relative to the out-of-plane FM ordering ($FM_\perp$) for various magnetic configurations of C_6O_6, C_6S_6, and C_6Se_6 for U_{eff}=0 eV (left panel) and U_{eff}=3 eV (right panel).

ligands are generally metallic. For the case of HITP, we can observe MS or I state with a sizable gap. Substituting HITP to other ligands, we expect the band gap size can also be controlled. Among them, $Co_3(C_6S_6)_2$ and $Co_3(C_6Se_6)_2$ are also quite interesting because they show BMS behavior. The spin-flip gap (Δ_{sf}), spin-flip energy in valence (Δ_2) and conduction (Δ_3) band is about 0.1 eV. This scale fits well with the requirements of BMS materials, which suggests that they could be suitable candidates for spintronics applications. When U_{eff}=3 eV was used, we see that most

materials show HM behavior. With increasing the effective Coulomb interaction on the metal site, the d bands across the Fermi level are pushed upward. Then, the remaining bands across the Fermi level become the ligand p_z bands, which can be seen in Fig. 4.5. We also see that the spin-gap in each channel ($\Delta_\uparrow$ and $\Delta_\downarrow$) can be controlled by the metal types. For example, $\Delta_\downarrow$ decreases from $1.47 \rightarrow 1.20 \rightarrow 1.00$ for $M_3(C_6S_6)_2$ system with U_{eff}=3 eV calculations. For fixed metal compound, we also see $\Delta_\downarrow$ decreases as $1.71 \rightarrow 1.47 \rightarrow 1.42$ for $Mn_3(C_6O_6)_2$, $Mn_3(C_6S_6)_2$, and $Mn_3(C_6Se_6)_2$. This suggests that bandgap tuning can be achieved by substituting the metal atom or ligand types. Since a varity of ligands can form M_3L_2 lattice, we expect desired gap size for the specific applications can be achieved by studying other ligands.

5.2 Effective Magnetic Interaction in Kagome MOFs

The magnetic orderings presented in Table 5.1 can be understood in terms of the effective model Hamiltonian of effective magnetic interactions in 2D Kagome lattice systems [77, 78, 79, 80, 81]. Since even the smallest ligand like $Fe_3(C_6S_6)_2$, as illustrated in Fig. 3.2, requires a higher order hopping process to get the effective magnetic exchange interactions between neighboring magnetic ions, the nearest-neighbor (NN) hopping model may be sufficient to describe the effective magnetic interactions in M_3L_2 MOFs. Indeed, the effective NN hopping between two metal atoms occurs along M $\rightarrow$L$\rightarrow$M. For the case of the smallest ligand such as $Fe_3(C_6S_6)_2$ (Fig. 3.2), this is already third order process (Fe $\rightarrow$ S $\rightarrow$ S $\rightarrow$ Fe). The effective hopping parameter t_{eff} between metal atoms from this nth order hopping is roughly $\bar{t}^n/\overline{\Delta}^{n-1}$, where $\bar{t}$ is the averaged hopping parameter between atoms and $\overline{\Delta}$ is the averaged excitation energy. Then, the effective exchange coupling J_{eff}

between two metal atoms roughly becomes

$$J_{\text{eff}} \sim \frac{\overline{t_{\text{eff}}}^2}{U} \sim \frac{\bar{t}^{2n}}{\overline{\Delta}^{2n-2}U}. \tag{5.1}$$

Thus, as the size of the ligand gets larger, the effective exchange coupling gets smaller. For example, our calculation shows that $J = -14$ meV for $Fe_3(HAB)_2$ and -4 meV for $Fe_3(HITP)_2$. Even though their structure is similar, the large ligand size of HITP suppresses even the NN hopping. It is possible to have a sizable next-nearest-neighbor hopping, but in MOFs, the ligand size is usually large enough to suppress all the hoppings other than the NN one. Thus, it is enough to consider only the NN Hamiltonian when discussing the magnetic properties of the MOFs system.

A spin Hamiltonian for the 2D Kagome lattice can be written as

$$H = \sum_{\langle i,j \rangle} J_{ij}\mathbf{S}_i \cdot \mathbf{S}_j + \mathbf{D}_{ij} \cdot (\mathbf{S}_i \times \mathbf{S}_j) + \sum_i A S_i^{z2} \tag{5.2}$$

where the sums are made between all the NN pairs $\langle i, j \rangle$. The first and second terms represent the isotropic and anti-symmetric exchange interaction between neighboring sites, and the last term represents the on-site anisotropy.

Under C_{3v} symmetry of the Kagome lattice, we can construct the symmetry-adapted spin configurations corresponding to different irreducible representations as shown in Fig. 5.2 [77]. Here we only consider the $\mathbf{q} = 0$ case for simplicity. Since J is usually larger than D in most cases, the sign of J determines either FM or AFM ground states. For FM ordering ($J < 0$), there are three possible configurations: one-dimensional representation of out-of-plane FM state ($FM_\perp$) and two-dimensional representation of in-plane FM states ($FM_\parallel$), where the sign of A determines the magnetic anisotropy. AFM ordering ($J > 0$) exhibits non-collinear orderings as labeled by one-dimensional representations of AFM A_1 and A_2, and

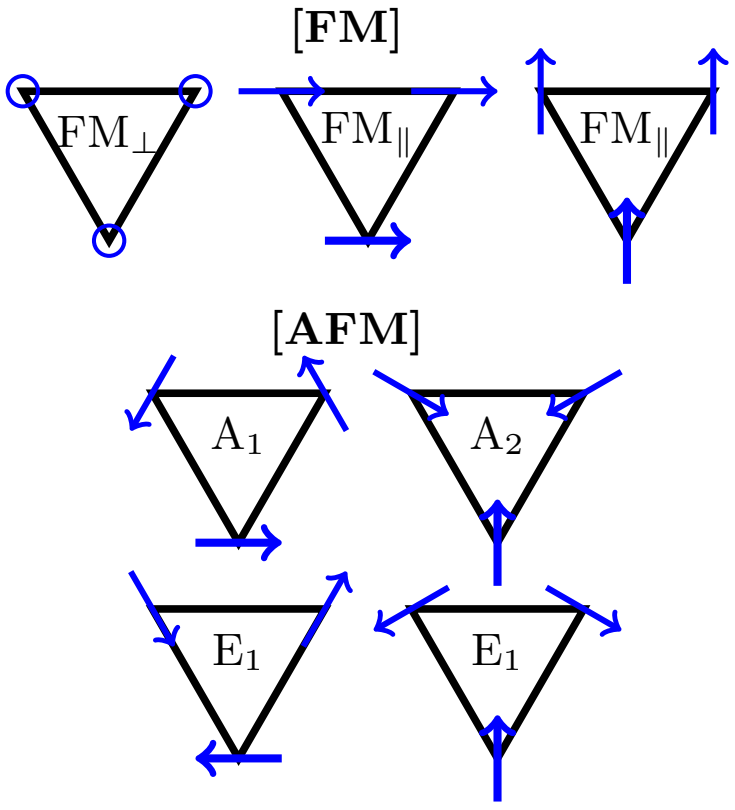

Fig. 5.2. Symmetry-adapted magnetic configuration in kagome lattice. Only $\mathbf{q} = 0$ states are shown.

two-dimensional representation of E_1. Two states A_1 and A_2 become degenerate for the isotropic Heisenberg model. The sign of D determines the AFM ground state between AFM_A and AFM_E.

Incidentally, there exist two more symmetry-adapted AFM E_2 states which incorporate out-of-plane spin components. For instance, the out-of-plane components (S_{z1}, S_{z2}, S_{z3}) of E_2 states are $(1, -1, 0)$ and $(1, 1, -2)$, respectively. Since these mixed-valence states were not observed in any system in our calculations, we will not include these states for further discussion.

The magnetic ground states listed in Table 5.1 match the symmetry-adapted configurations of Fig. 5.2. For each spin configuration obtained from DFT+U calculations, we can assign model parameters to the total energy as follows:

$$E_{FM_\perp} = E_0 + 6J + 3A \tag{5.3}$$

$$E_{FM_\parallel} = E_0 + 6J \tag{5.4}$$

$$E_{AFM_A} = E_0 - 3J - 3\sqrt{3}D \tag{5.5}$$

$$E_{AFM_E} = E_0 - 3J + 3\sqrt{3}D, \tag{5.6}$$

where E_0 is the total energy part independent of the spin configuration. Then, from the calculated total energies, we can determine the coupling constants of the effective magnetic Hamiltonian.

Another approach for calculating the parameters is through small tilting of spin angles. For instance, for the spin component of $\mathbf{S} = (0, 0, 1)$, if we tilt this spin along x-axis with small angle θ, the spin component becomes $\mathbf{S} = (\theta, 0, 1 - \frac{\theta^2}{2})$ ignoring the higher order terms. Then, the total energy can be expressed as follows:

Tilting	Energy
(0,0,0)	$E_0 = 6J + 3A$
(**x**,0,0)	$E = E_0 - 2J\theta^2 - A\theta^2 + O(\theta^3)$
(**x**,**x**,**x**)	$E = E_0 - 3A\theta^2 + O(\theta^3)$
(**x**,−**x**,0)	$E = E_0 - 4J\theta^2 + 2D\theta^2 - 2A\theta^2 + O(\theta^3)$

Here, the tilting direction represents along which direction the spins would be tilted with the initial $\mathbf{S} = (0, 0, 1)$ direction. Using DFT, we can calculate the energy variation with these small angles and extract the exchange parameters. Our calculation gives both approaches gives almost similar results. The calculated

parameters can be found in Table 5.4 and 5.5 The T_c values were calculated with the Monte Carlo method. We employed both Heisenberg and Ising Hamiltonian. The dependece of MC simulation on the supercell size L was measured by increasing L and calculating the Binder cumulant (Fig. 5.3 (a)) and heat capacity (Fig. 5.3 (b)). T_c of AFM configuration appears to be very small compared to FM case even with a similar $|J|$ value because of the existence of many degenerate co-planar states at low-temperature [81]

As illustrated in Fig. 4.3, the main feature of the NM insulating $Ti_3(C_6S_6)_2$ band structure is the presence of the strongly covalent $dp\sigma$-b_{1g} bonding state and the partially filled $dp\pi$-e_g bands across the Fermi level. The stability of the NM ground state arises from the covalent bonding of the Ti $3d$ b_{1g} states in hybridization with neighboring atoms in planar square coordination. Indeed, the covalent bonding character of the b_{1g} state is also prominent in the band structure of $Ni_3(C_6S_6)_2$, where all the other d levels of e_g, a_{1g}, and b_{2g} states are filled with both spin components. Therefore, it is evident that the NM character of $Ni_3(C_6S_6)_2$ can be understood from the same standpoint as $Ti_3(C_6S_6)_2$, namely, the strong covalent bonding of b_{1g}.

The coexistence of covalent and ionic bonding characters of $3d$ orbitals is a distinctive feature of the 2D M_3L_2 MOFs, as demonstrated in Fig. 4.6. For the series of $3d$ transition metal elements, the covalent b_{1g} bonding has no contribution to the local moment. In contrast, the localized d-orbital components such as a_{1g}, b_{2g}, and e_g states are responsible for the local magnetic moments. The stepwise increase of the a_{1g} and b_{2g} occupancy, marked by the filled triangle in Fig. 4.6, manifests the localized ionic character of a_{1g} and b_{2g} orbitals. On the other hand, the b_{1g} occupancy of both up-and down-spin components, marked by the filled

Table 5.4: Magnetic exchange parameters (meV) and T_c (K) with U_{eff}= 0 eV calculation. For FM ordering, results from the Ising Hamiltonian are also denoted in the parenthesis.

		V	Cr	Mn	Fe	Co
$M_3(C_6O_6)_2$	J	3.91	12.36	-23.73	-16.9	1.93
	D	0.01	0.19	-0.21	-0.12	0.37
	A	0.01	0.34	-0.55	0.43	0.10
	T_c	0.17	0.50	183 (585)	132 (422)	0.08
$M_3(HAB)_2$	J	12.73	13.42	-21.30	-12.43	-3.32
	D	-0.04	0.30	-0.02	1.13	0.86
	A	0.02	0.33	-0.55	-0.32	0.01
	T_c	0.52	0.55	157 (483)	106 (360)	25 (80)
$M_3(C_6S_6)_2$	J	3.46	24.38	-11.42	-10.30	-7.72
	D	0.00	0.15	0.10	0.07	-0.13
	A	0.00	0.14	-0.53	-0.19	0.83
	T_c	0.14	0.99	82 (280)	73 (270)	2 (7)
$M_3(C_6Se_6)_2$	J	2.42	13.10	-3.79	-5.69	-4.27
	D	-0.10	-0.10	0.40	0.10	0.05
	A	0.57	1.07	-1.33	-0.30	0.45
	T_c	0.09	0.51	20 (82)	44 (135)	23 (101)
$M_3(HITP)_2$	J	1.62	7.75	-5.02	-4.18	-2.68
	D	0.05	0.06	0.08	0.11	0.10
	A	0.10	0.19	-0.57	-0.38	0.38
	T_c	0.06	0.31	38 (137)	34 (118)	15 (60)

Table 5.5: Magnetic exchange parameters (meV) and T_c (K) with U_{eff}= 3 eV calculation. For FM ordering, results from the Ising Hamiltonian are also denoted in the parenthesis.

		V	Cr	Mn	Fe	Co
$M_3(C_6O_6)_2$	J	21.57	8.71	-21.66	-13.53	-0.48
	D	0.09	0.03	-0.13	-0.30	-0.15
	A	0.00	0.42	-0.57	0.55	0.00
	T_c	0.84	0.35	168 (521)	102 (313)	2.8 (9)
$M_3(HAB)_2$	J	10.16	13.88	-22.06	-11.56	-5.05
	D	-0.02	0.12	-0.03	0.11	0.57
	A	0.06	0.41	-0.61	-0.11	0.56
	T_c	0.41	0.56	174 (535)	88 (266)	37 (117)
$M_3(C_6S_6)_2$	J	23.99	23.41	-9.82	-10.35	-9.02
	D	0.11	0.15	0.10	-0.07	0.05
	A	0.23	0.40	-0.55	-0.28	1.34
	T_c	0.98	0.56	77 (235)	80 (253)	73 (224)
$M_3(C_6Se_6)_2$	J	14.93	27.56	1.42	-5.61	-6.64
	D	-0.17	-0.77	-1.18	0.16	-0.73
	A	0.68	1.06	-1.20	-1.08	0.95
	T_c	0.60	1.10	0.04	40 (126)	51 (160)
$M_3(HITP)_2$	J	0.94	18.24	-6.72	-4.57	-2.32
	D	0.02	0.30	0.10	-0.04	0.12
	A	0.00	0.37	-0.88	-0.21	0.28
	T_c	0.04	0.74	60 (187)	35 (102)	11 (54)

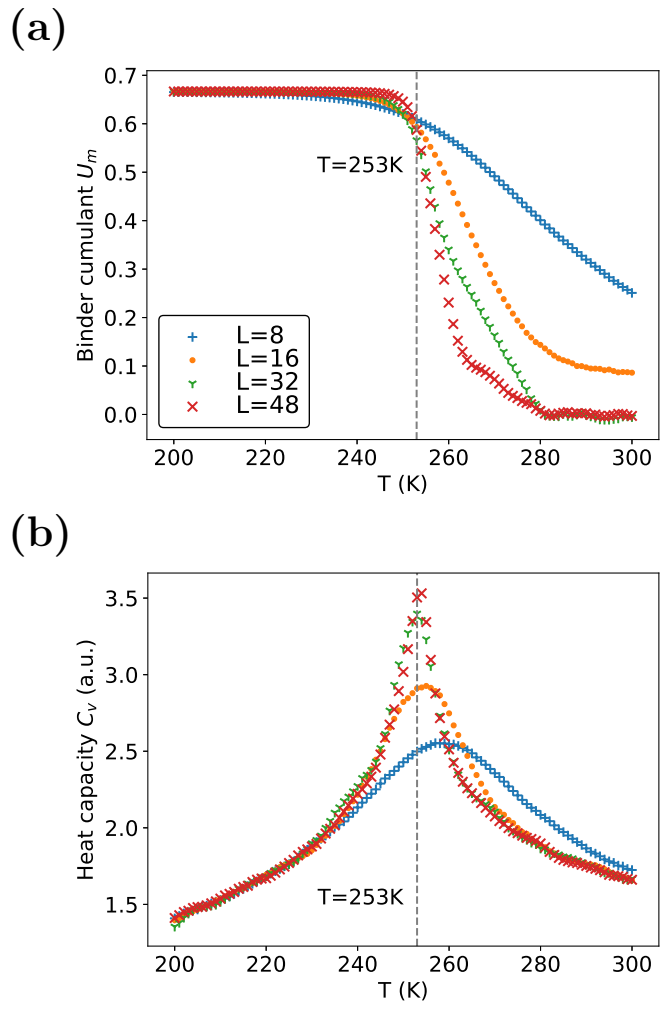

Fig. 5.3. Dependence of the results on the supercell size (L) in the MC simulation for $Fe_3(C_6S_6)_2$ with $J = -10.35$ meV employing Ising model. (a) Binder cumulant (b) heat capacity.

squares in Fig. 4.6, remains close to one throughout the series of M from Ti to Ni, demonstrating the nature of covalent bonding. Still, we can observe that the slight variation of the b_{1g} occupancy seems to reflect the degree of covalency depending on the combination of M and L. Further, despite the strong covalency, the b_{1g} states can be affected by the strong FM exchange interactions, leading to small induced spin polarization of the b_{1g} state.

Another captivating feature in Fig. 4.6 is the occupancy change of the $e_g^{*\uparrow}$ and $e_g^{*\downarrow}$ states throughout the series of M from Ti to Ni. The partial e_g^* occupancy means that either $e_g^{*\uparrow}$ or $e_g^{*\downarrow}$ bands lie across the Fermi level and may be responsible for the effective exchange interactions between neighboring transition metal sites. The band structures of $Ti_3(C_6S_6)_2$, $Cr_3(C_6S_6)_2$, and $Fe_3(C_6S_6)_2$ described in Fig. 4.3, 4.4, and 4.5, respectively, can be easily understood by the e_g^* bands contributing to the electronic structure near the Fermi level. This surprising appearance of the common e_g^* bands across the Fermi level is a consequence of the coexistence of covalent and ionic bonding characters of $3d$ orbitals in the series of M_3L_2 systems.

The e_g occupation in the AFM ground states of $V_3(C_6S_6)_2$ and $Cr_3(C_6S_6)_2$ appears to have almost full $e_g^{\uparrow}$ states with almost empty $e_g^{\downarrow}$. This feature is shown in the calculated PDOS of AFM $Cr_3(C_6S_6)_2$ of Fig. 4.4. Since the $e_g^{\downarrow}$ level is far above the Fermi level, only the $e_g^{\uparrow}$ level of the M site remains active and can contribute to the effective exchange interactions. On the other hand, the e_g occupations in the FM ground state of $Mn_3(C_6S_6)_2$, $Fe_3(C_6S_6)_2$, and $Co_3(C_6S_6)_2$ are characterized by the fully occupied majority-spin $e_g^{\uparrow}$ level with partially occupied $e_g^{\downarrow}$ levels. The partially occupied $e_g^{\downarrow}$ bands also appear in the calculated PDOS of FM $Fe_3(C_6S_6)_2$ of Fig. 4.5. The $dp\pi$ $e_g^{\downarrow}$ bands in the minority-spin channel split across the Fermi level. Thus, it is expected that the partially filled $e_g^{\downarrow}$ level of the M site becomes cru-

cial in determining the FM exchange interactions. To understand possible hopping processes between neighboring transition metal M sites via intermediate ligand L sites, we present a schematic configuration of the $e_g^{\uparrow}$ and $e_g^{\downarrow}$ bands relative to the ligand states in Fig. 5.4 for (a) AFM and (b) FM ground states.

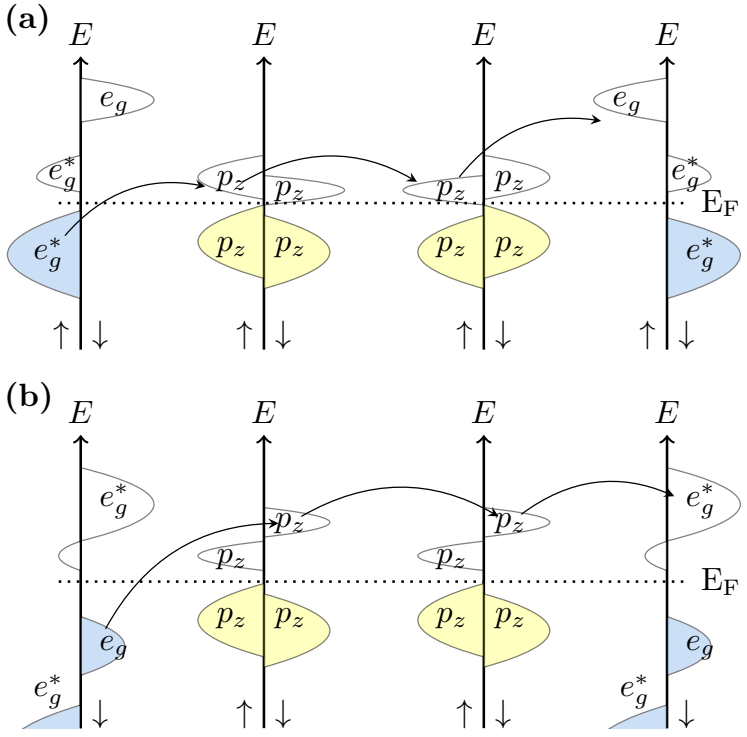

Fig. 5.4. Schematic description of superexchange mechanism between two metal e_g orbitals through ligand p_z orbitals for (a) AFM exchange and (b) FM exchange.

5.2.1 AFM ordering

Now we can examine a possible mechanism behind the AFM ground state of the Cr and V MOFs. To be specific, let us start from the electronic structure of $Cr_3(C_6S_6)_2$

illustrated in Fig. 4.4. As described in Sec. 4.2.2, the almost fully occupied $e_g^{*\uparrow}$ $dp\pi$ bands lie just below the Fermi level, while the $e_g^{*\downarrow}$ bands are empty. The $dp\pi$ hybridization between Cr d_{zx} and d_{yz} orbitals and ligand p_z states mediates a hopping process and consequently becomes responsible for the superexchange paths between neighboring transition metal ions. Since the e_g^* orbitals are the only d-orbitals contributing to the inter-site hopping via ligand states, we can identify the possible superexchange processes by considering the virtual hopping processes starting from the occupied $e_g^{*\uparrow}$ states.

One of the possible superexchange processes for this AFM exchange is schematically drawn in Fig. 5.4(a). Starting from the metal site, the electron in $|e_g^*, \uparrow\rangle$ state below Fermi level can be transferred to neighboring $|p_z, \uparrow\rangle$ hole state. If the spin configuration of two metal atoms is anti-parallel, there exists empty $|e_g, \uparrow\rangle$ so that the electron can be transferred through the $|e_g^*, \uparrow\rangle \rightarrow |p_z\rangle \rightarrow |p_z\rangle \rightarrow |e_g, \uparrow\rangle$ process. Consequently, by counting the AFM superexchange process, we can estimate the exchange parameter by $J \sim 2t_{dp}^4 t_{pp}^2/(\Delta_{CT}^4 U)$, where t_{dp}, t_{pp}, Δ_{CT}, and U represent the hopping integrals between $p-d$ and $p-p$ orbitals, charge transfer energy between pd orbitals, and electron-electron interaction among d orbitals.

To verify this idea, we construct a simple tight binding (TB) model with d_{yz}, d_{zx}, and p_z orbitals. Fig. 5.5 shows the band structure of $Cr_3(C_6S_6)_2$ system from the DFT (left) and TB (right) calculation. The marker in each band represents the magnitude of PDOS of d_{yz}, d_{zx} (blue) and p_z (orange) orbital. To reproduce the DFT band, we construct the TB hamiltonian including only d_{yz}, d_{zx}, and p_z orbitals of metal (M), C, and S atoms within Slater-Koster parametrization. DFT bands without weights and not appearing on TB bands correspond to the in-plane $dp\sigma$-hybridized bands. Comparing the TB band to $dp\pi$-projected DFT band, we

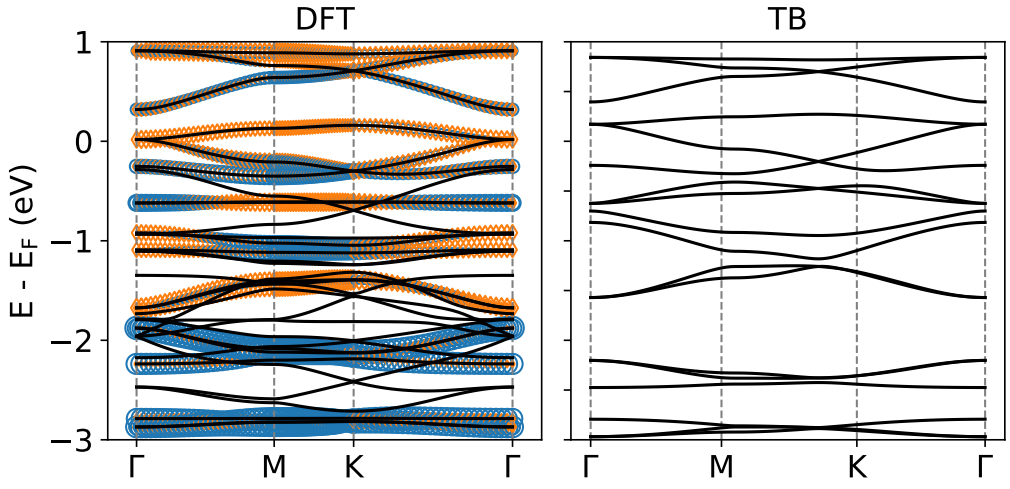

Fig. 5.5. (left) DFT band structure of $Cr_3(C_6S_6)_2$ with U_{eff}=3 eV calculation. The blue (orange) marker represents the magnitude of PDOS of d_{yz} and d_{zx} (p_z) components. (right) Tight binding band structure with d_{zx}+d_{yz}, and p_z orbitals.

get $t_{dp} = 0.91$, $t_{pp} = 0.23$, $\Delta_{CT} = 0.9$, and $U = 4.5$ eV. Substituting these values into J, we get $J = 20$ meV, which is consistent with the J values obtained from the total energy calculation. This verifies that the above superexchange is the dominant one.

If the spins were in FM configuration, we would have fully occupied (unoccupied) $|e_g^*, \uparrow\rangle$ ($|e_g^*, \downarrow\rangle$) state on both metal sites, respectively. In this case, the FM superexchange channel is not allowed because of the absence of an empty spin-$\uparrow$ channel. This situation is similar to the half-filled Hubbard model, which favors AFM ordering [82]. So, we have energy gain only for the anti-parallel configuration between metal atoms, which implies $J > 0$.

The frustrated Kagome lattice drives the AFM coupling into a non-collinear order for Cr and V MOFs. Our DFT calculations find the non-collinear order of

AFM_A or AFM_E, where the relative angle between each neighboring spin is 120°. The distinction between AFM_A and AFM_E ground states comes from the sign of the off-diagonal coupling D described in Eq. (5.3) and (5.6). A significant contribution to D comes from the spin-orbit coupling (SOC). We observe that AFM_A is the ground state in many cases except for $M_3(C_6Se_6)_2$. $V_3(HAB)_2$ is in AFM_E state, but the magnitude of D is small compared to J regardless of the magnitude of on-site Coulomb interaction. Thus, we can consider the AFM coupling in Cr MOFs as a typical case of the half-filled Hubbard model.

The exchange coupling mechanism in the Cr case can apply to the AFM coupling of V MOFs. The V atom has one less electron than Cr. Since the localized a_{1g} state of V d_{z^2} becomes empty, as shown in Fig. 4.6, the electron number change from Cr to V does not affect the basic configurations of the e_g^* bands near the Fermi level. The almost fully occupied $e_g^{*\uparrow}$ $dp\pi$ bands and the empty $e_g^{*\downarrow}$ remain intact and provide the same effective AFM superexchange interaction. However, we notice that the magnitude of AFM coupling significantly depends on the values of U_{eff} as shown in Fig. 5.1. When U_{eff}= 0 eV, the spin polarization of the e_g^* bands is significantly reduced, and its ground state is proximate to the nonmagnetic or weak FM ordering.

5.2.2 FM ordering

All the M_3L_2 systems with M = Mn, Fe, and Co favor FM ordering. However, as displayed in Table 5.1, some ligand types, e.g., $Co_3(C_6O_6)_2$ and $Mn_3(C_6Se_6)_2$ can lead to the AFM ground state. We examine the general mechanism behind the FM ordering and the exceptions, which provide an important clue to understanding the magnetism in these M_3L_2 systems.

Let us start from the electronic structure of $Fe_3(C_6S_6)_2$. As illustrated in Fig. 4.6, all the majority spin (spin-$\uparrow$) states are fully occupied except for the anti-bonding b_{1g} covalent states. In the spin-$\downarrow$ channel, the localized $b_{2g}^{\downarrow}$ state is fully occupied, and only the partially occupied $e_g^{*\downarrow}$ bands remains near the Fermi level. As discussed in Fig. 4.5, the active components of the band structure near the Fermi level are the $dp\pi$-hybridized $e_g^{*\downarrow}$ bands and the ligand S p_z bands. In contrast to the case of Cr, the $e_g^{*\uparrow}$ bands are fully occupied and stay well below the Fermi level. Instead, the $e_g^{*\downarrow}$ orbitals are the only d-orbitals contributing to the inter-site hopping via ligand states in $Fe_3(C_6S_6)_2$. Thus, we need to look for the possible superexchange processes by considering the virtual hopping processes starting from the occupied $e_g^{*\downarrow}$ states.

The virtual hopping paths for the FM exchange are illustrated in Fig. 5.4(b). An $e_g^{*\downarrow}$ electron at the metal site can hop to the neighboring metal site through ligand p_z states. In this case, the dominant hopping process is $|e_g^*,\downarrow\rangle \rightarrow |p_z,\downarrow\rangle \rightarrow |p_z,\downarrow\rangle \rightarrow |e_g^*,\downarrow\rangle$. Since the $e_g^{*\uparrow}$ states lie far below the Fermi level, the AFM exchange is suppressed compared to the FM exchange. After all, the FM exchange contribution becomes dominant when determining the effective magnetic exchange interactions. The FM exchange coupling J has a similar form as AFM exchange ($J \sim 2t_{dp}^4/\widetilde{\Delta}_{CT}^2\widetilde{U}$), where the $\widetilde{U}$ factor in the denominator represents the energy splitting between $|e_g^*,\downarrow\rangle$ states. The charge transfer energy $\widetilde{\Delta}_{CT}$ represents the energy difference between spin-down $p-d$ orbitals. A similar argument of this FM exchange on a partially filled orbital has been discussed in a doped semiconductor system [83, 84].

The FM exchange process of $Fe_3(C_6S_6)_2$ can apply to the Mn and Co cases. Since Mn has one less electron than Fe, the localized b_{2g} (a_{1g}) state of Mn (Co)

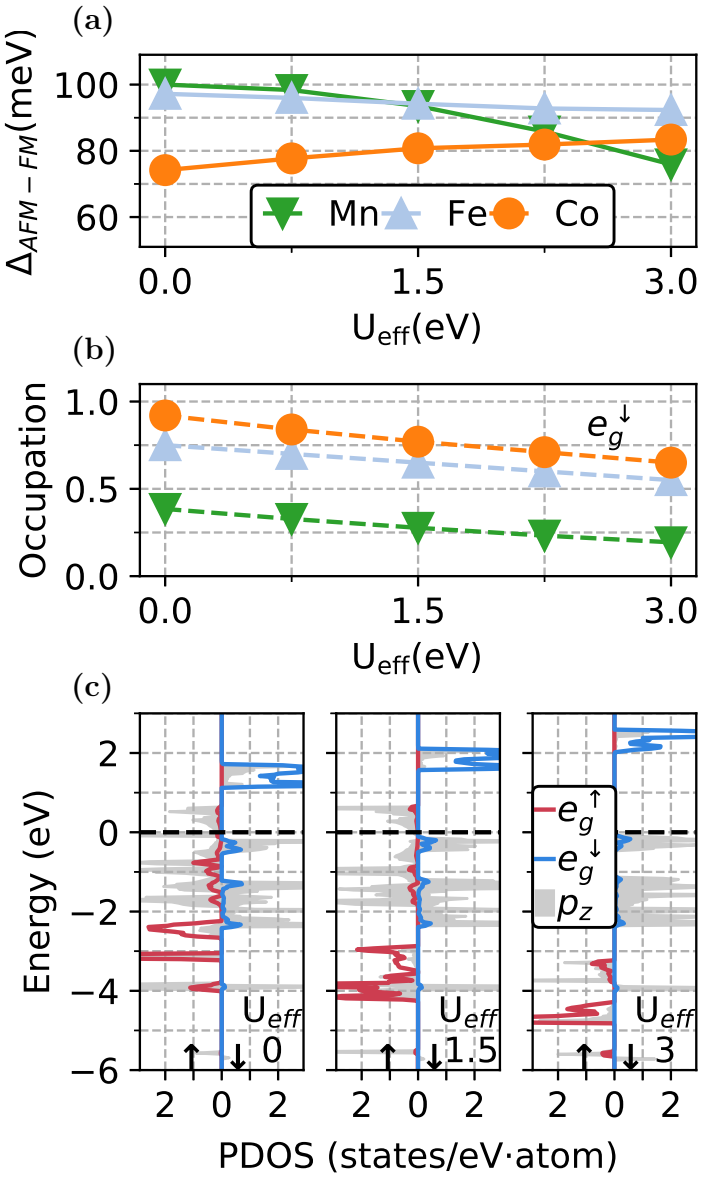

Fig. 5.6. U_{eff} dependence of (a) energy difference between AFM and FM states and (b) $e_g^{\downarrow}$ orbital occupation number of $Mn_3(C_6S_6)_2$, $Fe_3(C_6S_6)_2$, and $Co_3(C_6S_6)_2$ system. (c) PDOS of $Co_3(C_6S_6)_2$ system with various U_{eff} parameters.

becomes empty (occupied), as shown in Fig. 4.6. The change of d-occupation for Mn and Co does not affect the electronic configuration of $e_g^{*\downarrow}$ bands near the Fermi level except for the slight change of $e_g^{*\downarrow}$ band filling. Therefore, the FM exchange process based on the $e_g^{*\downarrow}$ states can apply to all the FM exchange interactions in the Mn, Fe, and Co M_3L_2 systems.

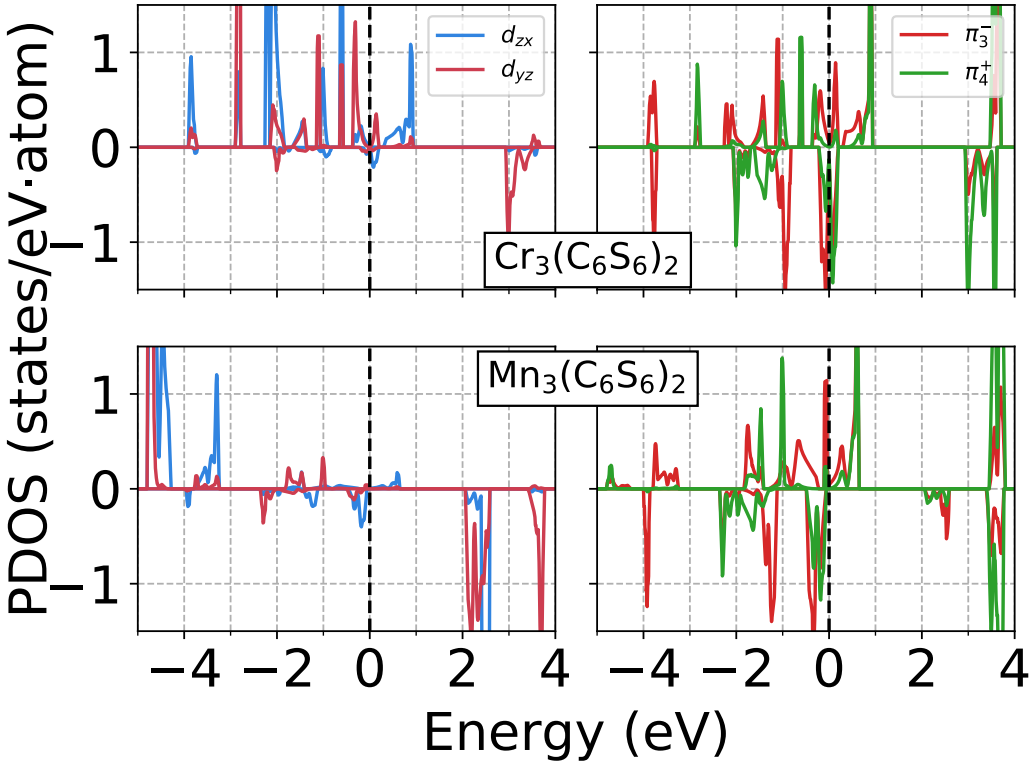

Fig. 5.7. PDOS of $Cr_3(C_6S_6)_2$ (top) and $Mn_3(C_6S_6)_2$ (bottom) system.

Here, one subtle issue is the change of magnetic ordering between Cr and Mn. As shown in Fig. 4.6, the d occupation does not significantly vary between Cr and Mn. We observe a slight increase of overall d electrons, but a significant change of d electron does not seem to occur even though Mn possesses one extra electron

than Cr. In this case, the ligand plays an important role. When changing the metal atom from Cr to Mn, the unoccupied ligand states in the spin-down channel get occupied. This can be verified in Fig. 5.7 shows the change of PDOS of Cr and Mn. We can see that the PDOS of d orbital, especially e_g orbitals, does not change that much. However, ligand p states right above the Fermi level (π_3 and π_4) gets occupied. The dominant hopping path of AFM superexchange is through the metal to ligand site as denoted in Fig. 5.4(a). When Cr is changed to Mn, the ligand hole spin state of the spin-down channel gets fully occupied, which suppresses the AFM superexchange.

To further investigate the FM superexchange mechanism, we monitor how the FM exchange coupling changes as the on-site Coulomb interaction parameter U_{eff} varies. Fig. 5.6 illustrates (a) the U_{eff}-dependence of the exchange coupling strength Δ_{AFM-FM}, i.e., the energy difference between AFM and FM phases, (b) the change of $e_g^{*\downarrow}$ band filling, and (c) the $e_g^{*\uparrow}$ energy levels as a function of U_{eff}. The change of Δ_{AFM-FM} seems roughly proportional to that of the $e_g^{*\downarrow}$ occupation, at least, in Mn and Fe systems. On the contrary, the Co Δ_{AFM-FM} exhibits the opposite behavior, that is, Δ_{AFM-FM} increases while the $e_g^{*\downarrow}$ occupation decreases. The Co case is distinguished from the other Mn and Fe cases regarding the strength of on-site exchange splitting.

To understand the different behavior of Co, we need to look into the strength of on-site exchange splitting of Co from those of Mn and Fe. Since the localized d orbitals have both spin-$\uparrow$ and spin-$\downarrow$ fully occupied, as shown in Fig. 4.6, the on-site exchange coupling at the Co site is relatively weak compared to that of Mn and Fe. Thus, the exchange splitting between $e_g^{*\uparrow}$ and $e_g^{*\downarrow}$ becomes small so that the center of Co $e_g^{*\uparrow}$ band is at around 2.5 eV when $U_{eff} = 0$ eV. However, the increase of U_{eff}

= 3 pushes the Co $e_g^{*\uparrow}$ level further down to 4.5 eV. Since the large separation of the $p-d$ levels enhances the suppression of the AFM exchange process, lowering the $e_g^{*\uparrow}$ level at the Co site strongly suppresses the AFM exchange contribution to the $\Delta_{\mathrm{AFM-FM}}$. Therefore, the $\Delta_{\mathrm{AFM-FM}}$ gets larger as U_{eff} increases due to the reduced AFM exchange contribution.

Although we cannot quantify all the parameters in the superexchange interactions, we may assert that the $\Delta_{\mathrm{AFM-FM}}$ is certainly positively correlated to the $e_g^{*\downarrow}$ occupation in the FM M_3L_2 systems. As evidenced by the Co $\Delta_{\mathrm{AFM-FM}}$ behavior, where the AFM exchange can still contribute to the $\Delta_{\mathrm{AFM-FM}}$, it is meaningful to identify the critical element for the FM exchange process.

We briefly mention Cu. Our calculation shows that Cu's magnetic interaction depends on the ligand's choice. C_6O_6, C_6S_6, and HAB show FM ground state, while C_6Se_6 is in NM order. HITP even shows AFM order. Cu is in $d^9\underline{L}^2$ configuration, so all the states except b_{1g} are fully occupied. The b_{1g} states are also isolated from other orbitals. Thus, the half-filled b_{1g} state suggests the AFM exchange would be favored. However, this b_{1g} state does not couple to p_z orbitals near the Fermi level as in previous cases, which means that the superexchange mechanism based on $dp\pi$ hybridization becomes very weak for this case. On the other hand, the itinerant p_z electrons also exist, which can contribute to FM coupling via Stoner ferromagnetism. These two factors compete with each other, and determining the exact ground state requires more detailed analysis for each ligand[85].

Another critical parameter in determining the FM exchange interactions is the metal-ligand hybridization. To examine the effect of the ligand on magnetic ordering, we plotted the change of d occupation of the Mn system by varying ligand from light (HAB) to heavy (C_6Se_6) ligand (Fig. 5.8). $e_g^{\uparrow}$ occupation does not vary

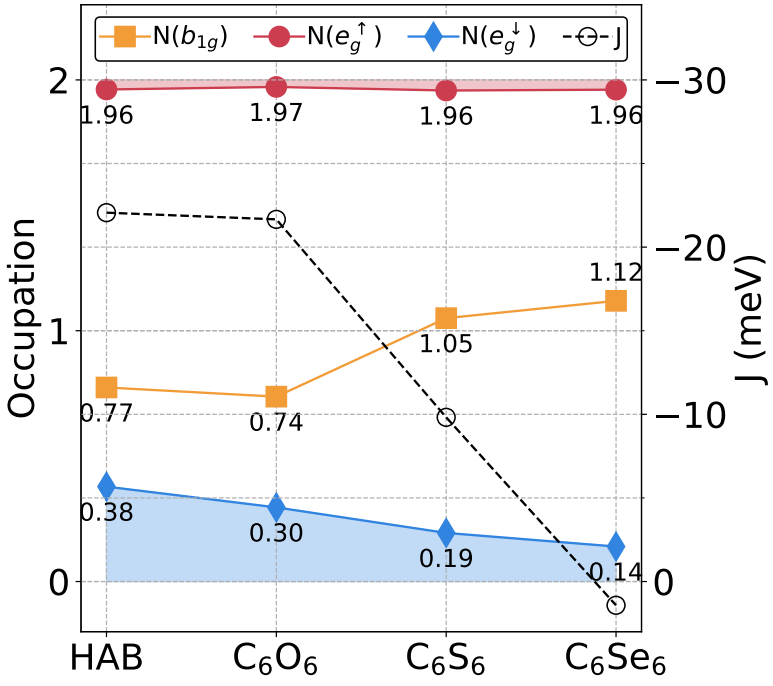

Fig. 5.8. Change of orbital occupation in Mn_3L_2 system with various ligand L. U_{eff}=3 eV was used for the calculation. Magnetic exchange parameter J is also shown.

by ligand type since it is already fully occupied. However, as the ligand gets heavier, we see a decrease of $e_g^{\downarrow}$ occupation. We also see that the exchange parameter J decreases and becomes AFM exchange for C_6Se_6. The $dp\pi$-hybridization gets weaker as the ligand gets heavier due to orbital mismatch, increasing the p-component on the bonding orbitals. For C_6O_6, we can see the sizable contribution of the e_g character on the central metal site. However, they decrease as the ligand gets heavier, and we see almost no contribution on C_6Se_6. Since the spin-down occupation plays an important role in the magnetic exchange, reducing this occupation decreases FM exchange. If we examine the occupation number of e_g orbitals (Fig. 5.8), we find that the occupation number of $e_g^{\downarrow}$ state is 0.14. Other cases show moderate $e_g^{\downarrow}$ occupations. So the FM coupling becomes very small with this low e_g occupation, and the AFM exchange could give a sizable contribution than the FM exchange. However, since the spin splitting energy is large, AFM contribution is also small, and their energy difference becomes negligible. Thus, MOFs with Mn generally show an FM ground state, ignoring this limiting case.

We also see an increase of b_{1g} occupation from 0.74 (C_6O_6) to 1.12 (C_6Se_6) as ligand gets heavier. This occurs because of the enhancement of the σ-donor character [86]. As going down chalcogen group O→S→Se, weak hybridization destabilizes the $dp\sigma$-bonding b_{1g} orbital, which enhances the σ-donor character. However, b_{1g} is a strong covalent bond, so increasing the d occupation on this state does not affect the magnetic exchange.

5.3 Magnetic Anisotropy

As discussed in the previous section, MOFs with Mn, Fe, and Co are generally in ferromagnetic ordering. Since these are 2D materials, it is important to have sizable

magnetic anisotropy energy (MAE) for long-range ordering.

As discussed in the previous section, MOFs with Mn, Fe, and Co are generally in FM ordering. For 2D materials, it is crucial to have sizable magnetic anisotropy energy (MAE) to sustain a long-range order. The magnetic ground state data (Table 5.2 and Table 5.5) shows that Mn and Fe generally have out-of-plane MAE ($FM_{\perp}$) while Co has in-plane MAE ($FM_{\parallel}$) regardless of the ligands. This result suggests that MOFs with Mn and Fe would be suitable for studying 2D FM behavior. We also see that the type of MAE does not significantly depend on U_{eff} values used in the calculations listed in Table 5.6.

Table 5.6: MAE (μeV) per metal atom of $Mn_3(C_6S_6)_2$, $Fe_3(C_6S_6)_2$, and $Co_3(C_6S_6)_2$ systems for U_{eff}=0 and 3 eV calculations.

U_{eff} (eV)	Mn	Fe	Co
0	528	195	-795
3	551	280	-1340

The MAE in this system is delicately connected to the spin and orbital structure near the Fermi level. In the second-order perturbation theory, the MAE contribution due to SOC hamiltonian of the metal atom ($H_{SOC} = \lambda \mathbf{L} \cdot \mathbf{S}$) can be calculated as

$$\text{MAE} = \lambda^2 \sum_{u,o,\sigma,\sigma'} \frac{|\langle o,\sigma|\mathbf{L}\cdot\mathbf{S}|u,\sigma'\rangle|^2}{E_{o,\sigma} - E_{u,\sigma'}} \tag{5.7}$$

where λ represents the SOC parameter for metal atom, o (u) for occupied (unoccupied) states, and σ, σ' for spin [87]. Within this formalism, the MAE is determined by the non-vanishing matrix elements $\langle u,\sigma'|\mathbf{L}\cdot\mathbf{S}|o,\sigma\rangle$ of ccoupied-unoccupied pairs, and their energy differences. As pointed out in Fig. 4.6, the localized d orbitals like a_{1g} and b_{2g} exhibit a discrete change of occupation number depending on the kind

of metal elements. This suggests that the change of MAE can be analyzed by examining the additional electron or hole state for a given metal atom. For instance, Fe has one additional hole state on a_{1g} orbital. Thus the change of MAE of Fe would arise from this state. For Mn, Fe, and Co, the major orbital characters near E_F are d_{zx} and d_{yz}. Thus, it is enough to analyze these orbitals' non-vanishing SOC matrix elements between the occupied and unoccupied states to determine MAE. If they give a similar contribution, then we further consider other contributions. Also, to distinguish the in-plane and out-of-plane spin orientation, we will denote $|\uparrow\rangle$ as the spin-up component when the quantization axis is chosen to be along [001](out-of-plane magnetization). At the same time, $|\rightarrow\rangle$ denotes spin-up component along [100](in-plane magnetization) from now on.

We first discuss the Co atom. Both U_{eff}=0 eV and U_{eff}=3 eV calculations show that Co possesses strong in-plane MAE (Table 5.6). Since the states near the Fermi level are composed of d_{zx} and d_{yz} orbitals, we identify which matrix elements vanish or contribute to MAE depending on the spin orientation. First, since both spin-up and spin-down channels of d_{xy} and d_{z^2} orbitals are fully occupied (Fig. 4.6), we can ignore contributions from these states. Now, we consider the unoccupied states of d_{zx} and d_{yz} orbitals. For in-plane spin case, two terms $\langle d_{yz}, \leftarrow |\mathrm{H_{soc}}| d_{xz}, \rightarrow\rangle$ and $\langle d_{xz}, \leftarrow |\mathrm{H_{soc}}| d_{yz}, \rightarrow\rangle$ give large contribution on MAE because each state is fully occupied. However, this is different for the out-of-plane case. For out-of-plane case, the SOC preserves the spin direction: the non-vanishing matrix elements for the two unoccupied states $|d_{xz}, \downarrow\rangle$ and $|d_{yz}, \downarrow\rangle$ are $|d_{yz}, \downarrow\rangle$ and $|d_{xz}, \downarrow\rangle$, respectively. However, as can be verified in the occupation matrix (Fig. 4.6), their occupation is much smaller than the fully occupied opposite spin states, so this low occupation contributes to smaller energy on out-of-plane MAE. This difference in occupation

number determines the MAE for Co, resulting in an in-plane FM state. The remaining contribution between d_{yz}, d_{zx} and $d_{x^2-y^2}$ gives a slight energy gain on MAE for the out-of-plane case, but since the difference between spin occupation for these orbitals is small, it does not change the MAE type.

Table 5.7: Non-vanishing SOC matrix element($\langle\alpha|\mathbf{L}\cdot\mathbf{S}|\beta\rangle \neq 0$) for given orbitals. $\uparrow(\rightarrow)$ represents the spin-up component when quantization axis is chosen to be along [001]([100]).

	Non vanishing elements			
$d_{yz},\downarrow$	$d_{xy},\uparrow$	$d_{xz},\downarrow$	$d_{x^2-y^2},\uparrow$	$d_{z^2},\uparrow$
$d_{xz},\downarrow$	$d_{xy},\uparrow$	$d_{yz},\downarrow$	$d_{x^2-y^2},\uparrow$	$d_{z^2},\uparrow$
$d_{yz},\leftarrow$	$d_{xy},\rightarrow$	$d_{xz},\rightarrow$	$d_{x^2-y^2},\leftarrow$	$d_{z^2},\leftarrow$
$d_{xz},\leftarrow$	$d_{xy},\leftarrow$	$d_{yz},\rightarrow$	$d_{x^2-y^2},\rightarrow$	$d_{z^2},\rightarrow$
$d_{z^2},\downarrow$		$d_{yz},\uparrow$, $d_{xz},\uparrow$		
$d_{z^2},\leftarrow$		$d_{yz},\leftarrow$, $d_{xz},\rightarrow$		
$d_{xy},\downarrow$		$d_{yz},\uparrow$, $d_{xz},\uparrow$	$d_{x^2-y^2},\downarrow$	
$d_{xy},\leftarrow$		$d_{yz},\rightarrow$, $d_{xz},\leftarrow$	$d_{x^2-y^2},\rightarrow$	

Next, we discuss the Fe atom. He has one less electron than Co, which gives almost similar occupation numbers on each orbital, so the previous discussion on in-plane MAE contribution still survives. However, we have an additional contribution on MAE by an empty state in d_{z^2} spin down orbital. As can be seen in Table 5.7, d_{z^2} couples to d_{zx} and d_{yz} orbitals. In this case, the out-of-plane case contributes more to MAE. For the out-of-plane case, the unoccupied state $|d_{z^2},\downarrow\rangle$ couples to two fully occupied states $|d_{xz},\uparrow\rangle$ and $|d_{yz},\uparrow\rangle$ with opposite spin. For the in-plane case, the unoccupied state $|d_{z^2},\leftarrow\rangle$ couples to one opposite spin orbital $|d_{xz},\rightarrow\rangle$ and one

parallel spin orbital $|d_{yz}, \leftarrow\rangle$ which has lower occupation number. So, in this case, d_{z^2} gives out-of-plane MAE. Also, the exact SOC matrix element carries $\sqrt{3}$ factor ($\langle d_{z^2}, \downarrow | \mathbf{L} \cdot \mathbf{S} | d_{xz}, \uparrow\rangle = \sqrt{3}$), so this term gives three times larger contribution on MAE. Thus, if we consider this term with the previously mentioned in-plane term, we expect that out-of-plane MAE would dominate the Fe case.

Now we discuss the Mn atom. Mn has one less electron than Fe and this makes empty occupation on $|d_{xy}, \downarrow\rangle$ orbital (Table 4.6). Since other occupation remains almost the same in the Fe case, these orbital occupations result in out-of-plane MAE. Then we consider the effect of unoccupied d_{xy} orbital. d_{xy} orbital provides three non-vanishing SOC matrix elements which couple with d_{yz}, d_{zx} and $d_{x^2-y^2}$ orbitals. The coupling with d_{yz} orbital does not contribute to MAE because both out-of-plane and in-plane cases couple to opposite spin, which gives the same MAE. We have a slight energy gain on out-of-plane MAE for the remaining two orbital contributions. The coupling with d_{zx} orbital gives out-of-plane MAE while that of $d_{x^2-y^2}$ gives in-plane contribution if we consider the opposite and parallel spin character. But since $|d_{xz}, \uparrow\rangle$ is fully occupied while $|d_{x^2-y^2}, \rightarrow\rangle$ is not, the out-of-plane case gets slight energy gain by this contribution. Thus, we expect the out-of-plane MAE would be enhanced than the Fe case.

Lastly, we briefly mention the V case. V is in AFM ground state, but examining its FM anisotropy helps us understand the role of orbital occupation on MAE in this system. As can be seen in Fig. 4.6, V has three d electrons in major spin channels, d_{xy}, d_{zx} and d_{yz}. As discussed in the previous paragraph, the two occupied orbitals(d_{zx} and d_{yz}) result in in-plane MAE. The remaining d_{xy} orbital slightly favors out-of-plane MAE through coupling with d_{zx} orbital, but if we consider the total occupation of these orbitals, we expect that the FM state with V would favor

in-of-plane MAE. Although we have not specified it explicitly, the SOC of ligands also gives a similar effect. From the Table 5.5, we observe that MAE of $M_3(C_6Se_6)_2$ shows relatively large value of anisotropy prameter A compared to other cases. In the above arguments on MAE, we have only included the SOC of metal atoms assuming weak SOC on ligand orbitals. However, when the system includes heavy ligands such as Se, the SOC effect on the ligand site also contributes to the MAE on the metal site. This can be analyzed in the same way as the metal case with an effective hopping channel, and in this geometry, the ligand SOC gives the same MAE energy as metal atoms.

Table 5.8: Change of MAE(meV) per unit cell by varying the magnitude of SOC parameter of the given atom with ligand C_6S_6.

	SOC multiplier			
	0.0	0.5	1.0	1.5
Mn	0.073	0.457	1.591	3.468
Fe	0.020	0.107	0.585	1.393
Co	0.004	-0.631	-2.490	-5.373

Since the perturbation theory also depends on the energy splitting between occupied and unoccupied states, the exact energy structure on each orbital should also be considered when discussing MAE. However, we have verified our calculation of MAE for various ligands (C_6O_6, C_6S_6, C_6Se_6, HAB, and HITP) that this general trend caused by d orbital occupation is preserved.

The main contribution to MAE comes from the metal atom. Table 5.8 shows the change of MAE by controlling the strength of SOC factor λ on the given atom. MAE by the ligand-only case ($\lambda = 0$) shows a very small MAE. By increasing

λ, both MAE increases with factor λ^2 by increasing *lambda*. Co shows a very small out-of-plane MAE by ligand-only case, but its in-plane MAE increases as we increase λ, which explains the metal contribution on in-plane MAE on Co.

Chapter 6

Topological properties

In this chapter, we discuss the topological properties of some selected M_3L_2-type kagome MOFs. One of the unique features of kagome lattice is the existence of the dispersionless flat band. Electron correlation plays a significant role in this band. When this flat band carries nontrivial Chern numbers, it has been suggested that they could be a promising candidate for the realization of fractional Chern insulator[88, 89].

Our calculations reveal that suitable choices of ligand and metal could result in a nontrivial topological electronic structure. We suggest MOFs with Mn and Fe as a suitable system for studying topological properties since they experience a quantum phase transition by tuning electron correlation and becoming a Chern insulator. We explain the mechanism of this phase transition by Wannier function analysis and model Hamiltonian.

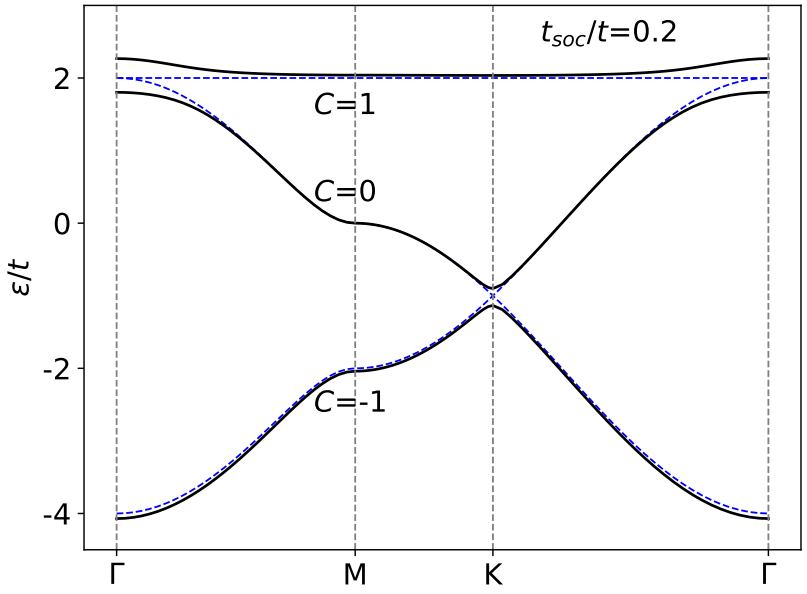

Fig. 6.1. Typical band structure on kagome lattice with NN hopping. Blue (black) line represents the band structure without (with) t_{soc} term. The Chern numbers (C) of each band are also shown.

6.1 Kagome Band Structure

The simplest model Hamiltonian describing the electronic structure of kagome lattice can be written as

$$H = -t \sum_{\langle i,j \rangle} c_i^\dagger c_j + i t_{soc} \sum_{\langle i,j \rangle} c_i^\dagger c_j, \tag{6.1}$$

where t (t_{soc}) is the spin-independent (SOC-induced) hopping parameter, $c_i^\dagger, c_i$ is an creation and annihilation operator for an electron on site i, and the summation is done over the nearest neighbor pairs. The Hamiltonian can be easily solved through Fourier transformation of c_i to $c_{\mathbf{k}}$. The corresponding electronic band structures for both $t_{soc} = 0$ (blue) and $t_{soc}/t = 0.2$ (black) cases are shown in Fig. 6.1. First,

we examine the case without SOC term. The overall band structure resembles graphene, which has two atoms in the unit cell and makes a honeycomb lattice. The major difference is that we have an additional flat band over the Brillouin zone. This dispersionless band arises from the unique structural properties of the kagome lattice [90]. In kagome lattice (Fig. 3.2), each hexagon is connected by a single atom We can regard the whole kagome lattice as a combination of multiple hexagons and their linker atoms. Let us consider the s-like orbital and the anti-bonding state on a hexagon. The hopping between hexagons becomes suppressed by the destructive interference between the anti-bonding state and linker atoms. The hybridization between these localized states is perfectly suppressed if we ignore the next-nearest neighbor hoppings and get the flat band.

The unique feature of this dispersionless band is that the charge carriers possess a zero group velocity and an infinite effective mass. Unlike the system with dispersive bands, the kinetic energy goes zero for this flat band system, and the major energy scale dominating the low energy physics is the electron-electron interaction. This many-body interaction induces a novel phenomena such as flat band ferromagnetism [91, 92, 93], superconductivity [94, 95, 96, 97], anomalous Quantum Hall effect [98, 99], fractal geometries [100, 101], and Wigner crystalization [102, 103, 104].

Another interesting point in the kagome system is its intrinsic topological bands. When we turn on the SOC effect, we see gaps at Γ and K points open up, and the system becomes an insulator. However, each band carries a finite Chern number of $1, 0, -1$, respectively, suggesting that they become Chern insulators. Unlike the graphene system, which requires the next nearest neighbor hoping to induce some topological properties[105], even with this simple tight-binding model with NN

term, we can induce the Chern insulating phase in the kagome system.

6.2 Nontrivial Electronic Structure

Among the various MOFs we have discussed, a ferromagnetic ground state was observed for MOFs with Fe, Mn, and Co. Especially, MOFs with Fe and Mn showed out-of-plane magnetic anisotropy for most cases (Table 5.6). In 2D systems, Mermin–Wagner theorem states that the long-range magnetic order is suppressed by thermal fluctuation [106]. One way of bypassing this constraint is the presence of magnetic anisotropy. This suggests that MOFs with Fe and Mn could be good candidates for 2D ferromagnetic materials. We look at $Fe_3(C_6S_6)_2$ sytsem as an example case.

Fig. 6.2 shows the electronic band structure and PDOS of $Fe_3(C_6S_6)_2$ with U_{eff}=3 eV calculation. Both metal and ligand PDOS are drawn. As discussed, the conduction band comprises metal d_{zx}, d_{yz} orbitals, and ligand p_z orbitals. For $Fe_3(C_6S_6)_2$, we see that a nearly flat band arises near the Fermi level for the spin-up channel. This is the result of spin-polarized calculation, and if we turn on the SOC coupling, the gap at the Γ point opens up a gap of size 0.5 meV.

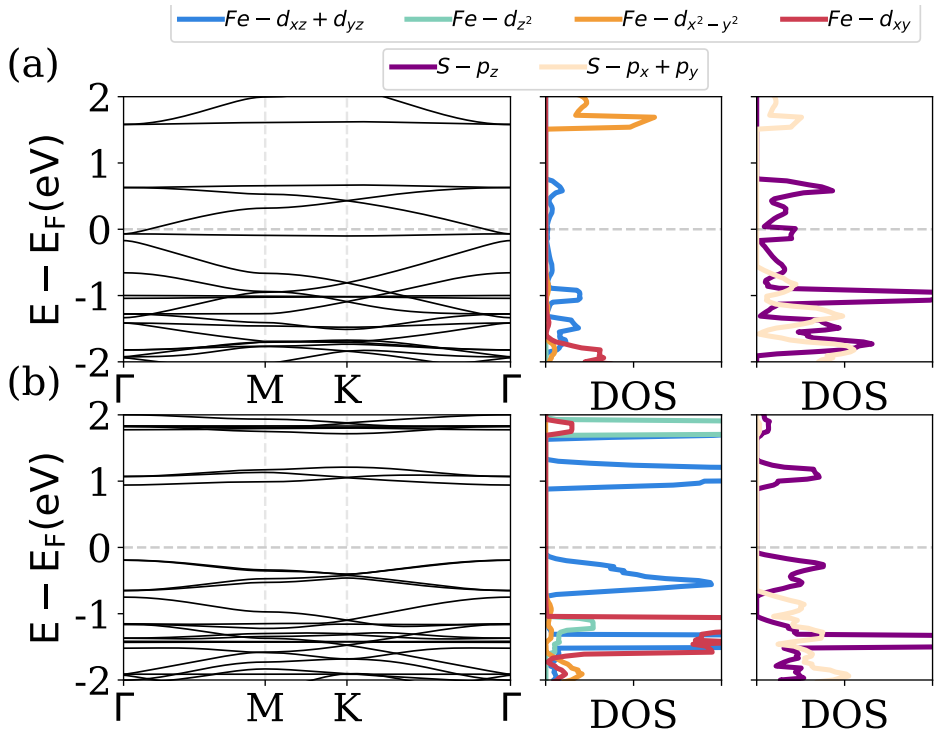

Fig. 6.2. Band structure and PDOS of $Fe_3(C_6S_6)_2$ with U_{eff}=3 eV. (a) Spin-up channel, (b) Spin-down channel. PDOS of metal *d* orbital and ligand *p* orbitals are shown.

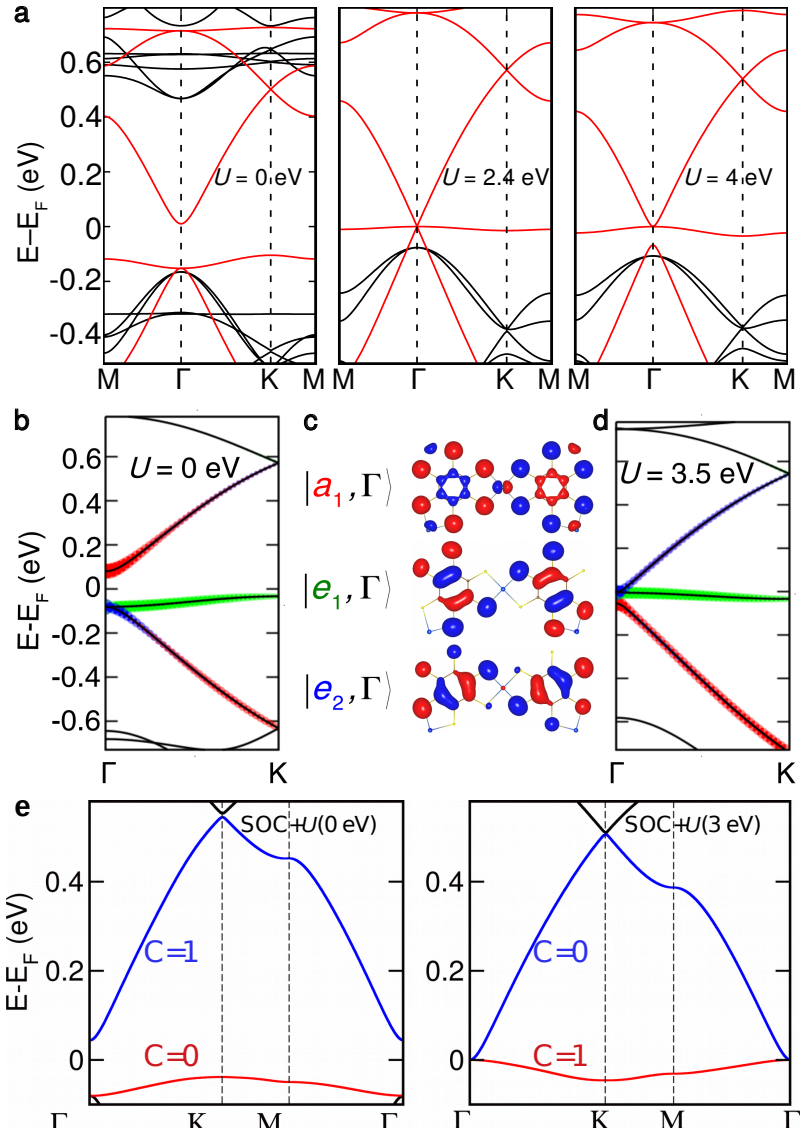

Fig. 6.3. (a) Electronic band structure of $Fe_3(C_6S_6)_2$ with respect to U. spin-up(spin-down) channel is represented with red(black) line. (b) Relative weight of $|a_1\rangle, |e_1\rangle$, and $|e_2\rangle$ near Γ point. (c) Shape of molecular orbital of $|a_1\rangle, |e_1\rangle$, and $|e_2\rangle$. (d) Relative weight each state with U_{eff}=3.5 eV calculation. (e) Chern number of each band near Fermi level for U+SOC calculation with U_{eff}=0 eV and 3 eV.

The interesting phenomenon occurs when we tune the Coulomb interaction strength U_{eff}. Fig. 6.3 (a) shows the electronic band structure near E_F. In this figure, the red (black) line represents the band structure for the spin-up (spin-down) channel. The spin-down band remains almost the same even if we increase U_{eff} from 0 to 4 eV. The unoccupied spin-down band gets only pushed upward.

We see a significant band structure change near Γ when we tune the electron correlation U_{eff}. For U_{eff}=0 eV case, the conduction band minimum occurs at Γ point. Two degenerate states exist below this level with a gap size of about 0.18 eV. However, as we increase U_{eff} value, these two levels are pushed upward, and they touch the conduction band minimum when U_{eff} reaches about 2.4 eV. If we further increase U_{eff} value, these two levels lie near E_F. Since the electron number is fixed, the lower-lying flat band right below the Fermi level is unoccupied in this case. Thus, with a strong U_{eff} value, we have a nearly flat band right below the Fermi level, which is degenerate at Γ point.

We first inspect why this band inversion occurs by examining the orbital characters. Fig. 6.3 (c) shows the wavefunction of three energy levels near E_F at Γ point. Under the C_3 symmetry of the lattice, we have a single $|a_1\rangle$ orbital and doublet $|e_1\rangle$ and $|e_2\rangle$ states. The major difference between these states is the electron occupation on the metal site. On the $|a_1\rangle$ orbital, we can see a clear electron occupation on the metal site. They are d_{zx} orbital. But for $|e_1\rangle$ and $|e_2\rangle$ orbitals, we do not have any electron occupation on metal site. The Coulomb interaction U_{eff} is only applied on metal d orbitals. Thus if we change the value of U_{eff} , only the energy level of $|a_1\rangle$ state would be affected. Thus, the change of $|a_1\rangle$ energy level induces the band inversion. This can also be verified by inspecting the orbital-projected band structure. Fig. 6.3 (b) and (d) shows the orbital-projected band structure. The red,

green and blue circle represent $|a_1\rangle$, $|e_1\rangle$ and $|e_2\rangle$ component, respectively. We can see that the $|a_1\rangle$ component (red circle) gets inverted with increasing U_{eff} value. The detailed mechanism of this band inversion will be invested with a tight binding analysis in the next section.

Since the band inversion is a crucial ingredient in inducing the topological phase transition, we can expect that the topological character would be changed with U_{eff} values. We can also induce a gap at Gamma point by including SOC interaction. Fig. 6.3 (e) shows the calculated Chern number of each band. When U_{eff}=0 eV, the Chern number C of the flat band below the Fermi level is 0, while the nontrivial band with C=1 occurs on the conduction band. Thus, the whole system becomes a trivial insulator. With increasing U_{eff}, the band inversion occurs, and the nontrivial contribution from the conduction band is transferred to this flat band. In this case, we get C=1 for the valance band, and the whole system becomes the nontrivial Chern insulator.

We calculate other physical quantities that can support this system's nontrivial nature. Ignoring the extrinsic contribution, the intrinsic anomalous Hall conductivity (AHC) σ_{xy} can be calculated from the electronic band struture as follows:

$$\sigma_{xy} = -\frac{e^2}{h} \int_{BZ} \frac{d^3k}{(2\pi)^3} \sum_n f_{nk} \Omega_{xy,nk} \tag{6.2}$$

where $\Omega_{xy,nk}$ is the Berry curvature and f_{nk} is the Fermi-Dirac distribution function. The summation is done for all bands. This formula implies that if we have a strong Berry curvature contribution that can occur with band inversion, we can have a high AHC signal. Also, since the integration of Berry curvature on a fully occupied band gives the Chern number an integer, the AHC signal calculated by varying the Fermi level should give a step-wise signal.

Fig. 6.4 (b) shows the AHC signal by varying the Fermi level. We can see that

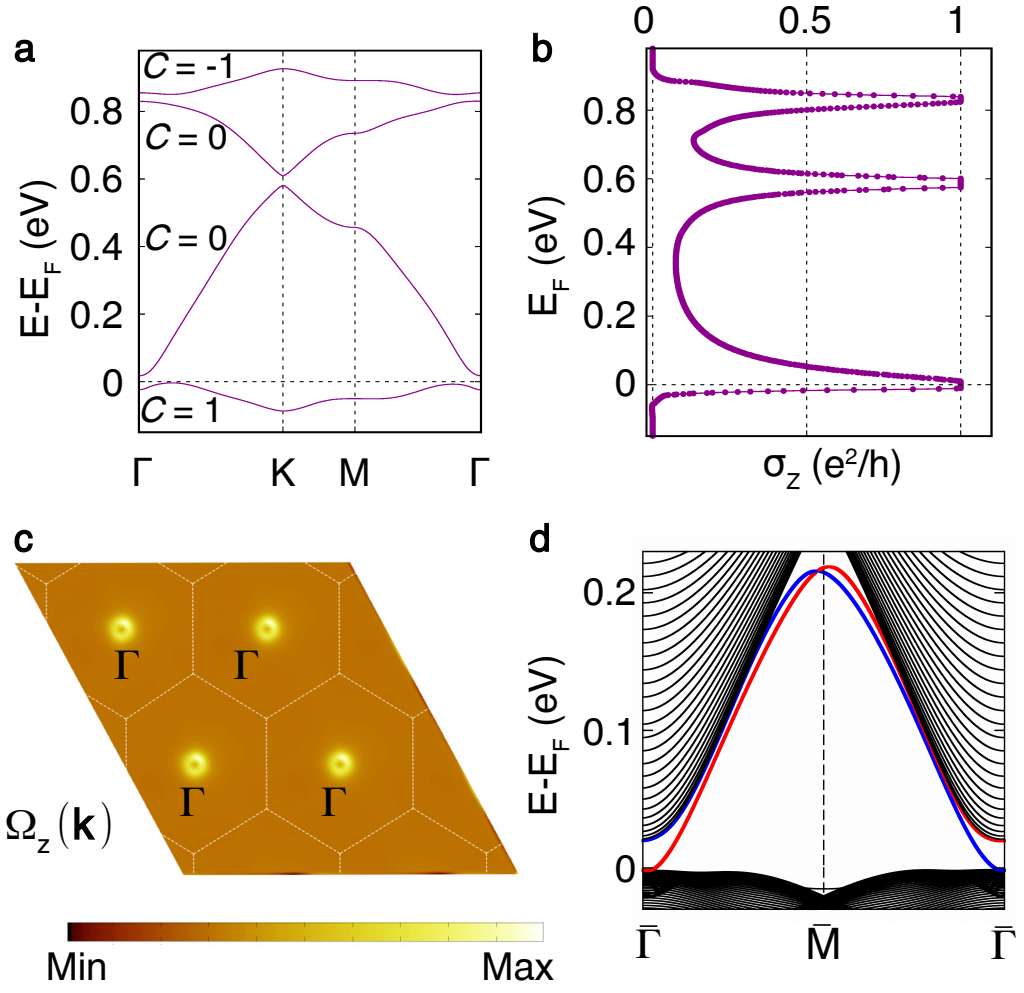

Fig. 6.4. (a) Band structure of $Fe_3(C_6S_6)_2$ with HSE06 + SOC calculation. The band gap at Γ point reaches about 23 meV. The Chern number C of each band is also shown. (b) The anomalous Hall conductivity σ_{xy} with variation of Fermi level. (c) The Berry curvature in thye Brillouin zone. (d) Band structure of finite system. The left (red) and right (blue) represent the edge state.

σ_{xy} reaches 1 (in units of e^2/h) and gives a small plateau near the Fermi level. This corresponds to the $C = 1$ result. If we further increase the Fermi level, σ_{xy} becomes a non-integer value, and it becomes an integer value again when the Fermi level lies behind the band gap. When these bands are fully occupied (E_F being above 0.8 eV), the total Chern number becomes zero, and the AHC also reaches zero. These results suggest that the system is a $C = 1$ Chern insulator.

As indicated in the previous paragraph, the band inversion mainly occurs at Γ point by tuning U_{eff} value. This inverted energy level contributes significantly to the Berry curvature, and we can see that Ω_{xy} has the largest contribution near Γ point (Fig. 6.4 (c)).

Another unique feature of the Chern insulator is the conducting edge state. According to the topological band theory, it is known that the Chern number corresponds to the number of the chiral edge states. For example, a Chern insulator with $C = 1$ carries conducting edge state of one e^2/h conductivity. In other words, the experimental way of identifying the Chern insulator phase is to very the presence of the chiral edge states at the boundary. Since the Chern number of both $Fe_3(C_6S_6)_2$ and $Mn_3(C_6S_6)_2$ are 1, we should observe the edge with a finite system. We calculated the edge band structure using the Wannier function basis with an iterative Green's function approach. Fig. 6.4 (d) shows the band structure of $Fe_3(C_6S_6)_2$ with U_{eff}=3.5 eV calculation in ribbon geometry. The red (blue) state represents the chiral edge state on the left (right) edge. We can see that they connect the valence and conducting band while no other states exist between the band gap. This conducting edge state confirms that this system is in Chern insulating states with $C = 1$.

6.3 Tight-binding Analysis

The topological phase transition between the Chern insulator and normal insulator discussed in the previous chapter occurs by the band inversion near the Fermi level. In this section, we construct a tight-binding Hamiltonian to get insight into the origin of the band inversion process.

The simple tight-binding Hamiltonian of $M_3(C_6S_6)_2$ can be written as follows:

$$H = \sum_{<\mathbf{r}\alpha,\mathbf{r}'\beta>} V_{\mathbf{r}\alpha,\mathbf{r}'\beta} c^{\dagger}_{\mathbf{r}\alpha} c_{\mathbf{r}'\beta} + \sum_{\alpha} \lambda_{\alpha} \hat{L_{\alpha}} \cdot \hat{S}_{\alpha} + \sum_{\mathbf{r},\alpha,\tau,\tau'} [\mathbf{B}_{\text{eff}}(\mathbf{r}) \cdot \boldsymbol{\sigma}]_{\tau,\tau'} c^{\dagger}_{\alpha,\tau,\mathbf{r}} c_{\alpha,\tau',\mathbf{r}} \quad (6.3)$$

Here, $V_{\mathbf{r}\alpha,\mathbf{r}'\beta}$ represents the Slater-Koster parameter, $\mathbf{r}, \mathbf{r}'$ for site index and α, β for orbital index. Since the orbital components near Fermi level are composed of metal d_{zx}, d_{yz} and ligand p_z orbitals, we only include these orbitals in the tight binding model.

The first term represents the spin-independent hopping Hamiltonian. In this model, we restrict the hopping process to be within the nearest neighbor atoms, which is typical when dealing hybridization of 3d transition metals. The second term sets the SOC for p and d orbitals. We only consider the onsite SOC effect. The last term describes the effective Zeeman field, which simulates the magnetic ordering of the system. For out-of-plane ferromagnetic system, we can simply set $\mathbf{B}_{\text{eff}} = B\hat{z}$. This term also sets the exchange energy between two spin channels.

With this model, we first consider $\lambda_{\alpha} = \mathbf{B} = 0$ case, which describes the energy dispersions of spinless system.

Fig. 6.5 shows the band structure of tight binding model by varying Fe-S hopping parameter $V_{pd\pi}$. Other parameters such as S-S, S-C, and C-C hoppings are set to be 0.25, 1.9, and 3 eV, respectively. First, we concentrate on the four conduction bands above the Fermi level. As in the DFT calculation with U_{eff}=0 eV (Fig. 6.3

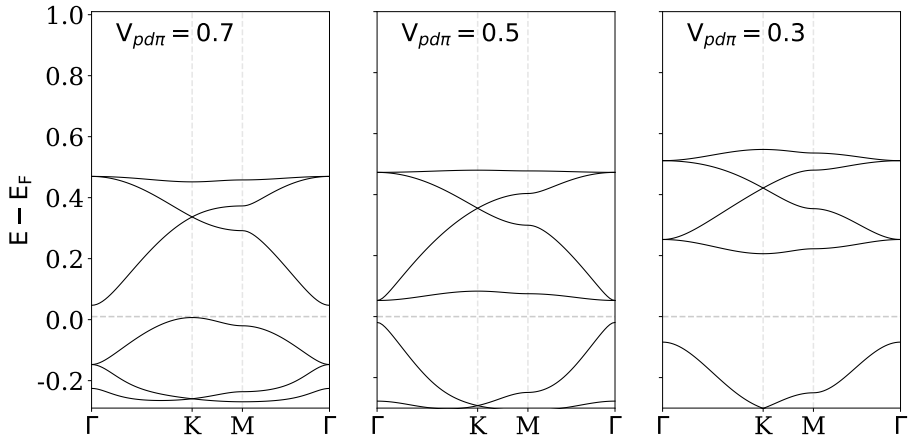

Fig. 6.5. Band structure of $Fe_3(C_6S_6)_2$ with tight binding Hamiltonian. $V_{pd\pi}$ represents the hopping parameter between Fe and S. Other parameters are set to be 0.25, 1.9, and 3 eV for S-S, S-C, and C-C hoppings, respectively.

(a)), we can observe three valance bands above the Fermi level with $V_{pd\pi}$=0.7 eV. If we decrease $V_{pd\pi}$, we observe that the energy of the topmost band below the Fermi level gets closer to the conduction band and gets inverted (Fig. 6.5). Decreasing this value further makes the flat band.

Thus, we observe that decreasing metal-ligand hopping parameter $V_{pd\pi}$ induces a similar band inversion effect like increasing U_{eff} value in DFT calculation. This phenomenon is related to the renormalization of the hopping parameter with U_{eff}. As mentioned in the previous section, the d level occupations of valance bands is different for $|a_1\rangle$ and $|e_1\rangle, |e_2\rangle$ states. Only $|a_1\rangle$ state has d level occupation. Increasing U_{eff} affects to this d state and induces band inversion. However, we can regard this effect as decreasing hopping parameters. Increasing U_{eff} parameter means we include the electron correlation effect on the metal d orbitals. Since the

electron-correlation is included on the metal site, the effective hopping with d level decreases ($t_{eff} \sim V^2/\Delta_{pd}$). This means U_{eff} has a similar effect of decreasing the hopping parameter in the tight-binding model.

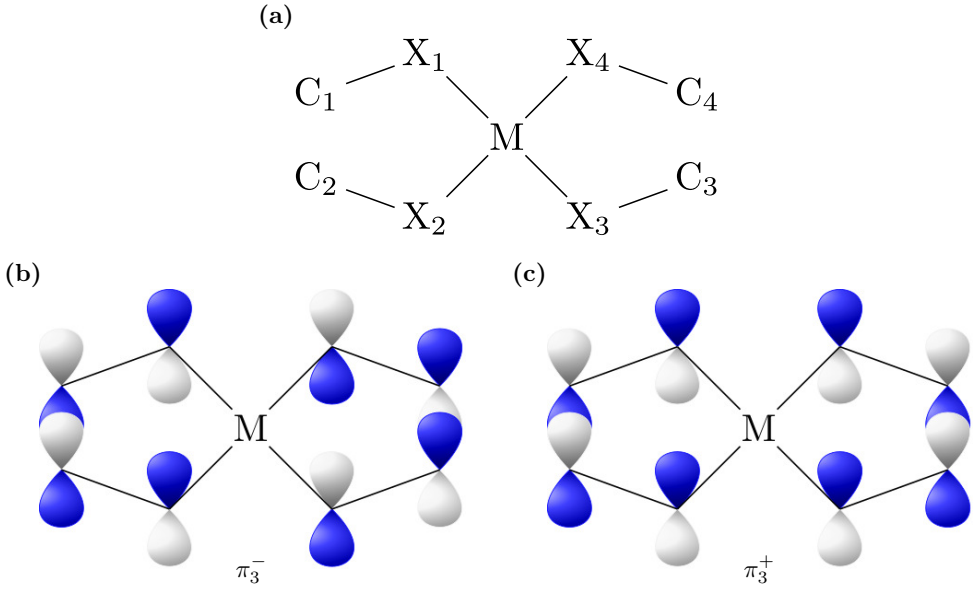

Fig. 6.6. (a) Local geometry around metal atom. (b) Out-of-phase and (c) in-phase combination of π_3 state.

The existence of energy states of almost the same energy, with one having a d component and one without a d component, is a general picture in this system. For the analysis of the ligand-effect, it is instructive to construct the full ligand orbitals near metal atoms[107]. Fig. 6.6 (a) shows the local geometry about metal site including the nearest chalcogen (X) and carbon (C) atoms. The site symmetry of metal is C_{2v} or D_{2h} depending on the atomic distortion. In this geometry, we can construct eight ligand orbitals with p_z orbitals, and the sign of each p_z orbital is shown in Table 6.1. In these orbitals, the superscript $-(+)$ means the in-phase(out-

of-phase) combination of left and right ligand to the metal atom. For instance, Fig. 6.6 (b) represents the out-of-phase combination of (X_1, X_2)-(X_3, X_4) orbitals, while Fig. 6.6 (c) represents the in-phase combination of those orbitals.

Among these constructions, only π_n^- orbitals can couple with metal d_{zx} and d_{yz} orbitals due to symmetry. Specifically, π_1^- and π_3^- mainly couples to d_{zx} while π_2^+ and π_4^+ couples to d_{yz} considering their orientation. In this combination, the energy of d_{yz} orbital lies slightly higher than d_{zx} due to the ligand energy difference ($E(\pi_1) < E(\pi_2) < E(\pi_3) < E(\pi_4)$).

Table 6.1: Sign of the p_z orbital in ligand π orbital with atomic coordination shown in Fig. 6.6(a)

	X_1	X_2	X_3	X_4	C_1	C_2	C_3	C_4
π_1^-	+	+	−	−	+	+	−	−
π_2^+	+	−	−	+	+	−	−	+
π_3^-	+	+	−	−	−	−	+	+
π_4^+	+	−	−	+	−	+	+	−
π_1^+	+	+	+	+	+	+	+	+
π_2^-	+	−	+	−	+	−	+	−
π_3^+	+	+	+	+	−	−	−	−
π_4^-	+	−	+	−	−	+	−	+

Fig. 6.7 shows the PDOS of $Fe_3(C_6O_6)_2$. We see that spin-up bands of d_{zx} and d_{yz} orbitals are fully occupied. Due to their low energy, these orbitals mainly couple with π_1 and π_2. These two ligand orbitals are almost fully occupied, so they do not contribute to magnetic exchange.

On the other hand, we can see the partial occupation of the spin-down band of

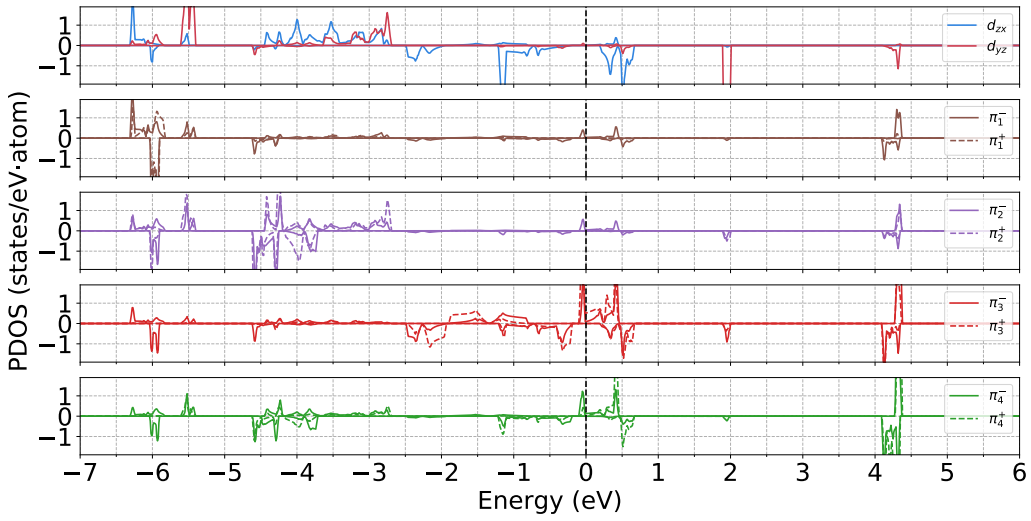

Fig. 6.7. PDOS of metal e_g states and ligand π orbitlas defined in Table 6.1. Dashed (dotted) line represents the out-of-phase (in-phase) combinations.

d_{zx} orbital around $-2 \sim 0$ eV. The hybridization of this d orbital comes from π_3^- and π_4^+ orbitals.

Fig. 6.8 shows the change of PDOS of Fe-d_{zx},d_{yz} and ligand-π_3^-, π_4^+ orbitals by changing chalcogen atoms from O $\rightarrow$ S $\rightarrow$ Se. As the metal-ligand hybridization increases, the d component under the Fermi decreases while the ligand p component increases.

The relation between hopping strength and the band inversion suggests how we can manipulate the band inversion process. The topological phase transition occurs with increasing $\mathrm{U_{eff}}$ or decreasing $V_{pd\pi}$. It means that the Chern insulator phase can be observed with a weak metal-ligand hybridization system. Electron correlation strength decreases as we go down through the periodic table. Also, as the atomic radius increases, the hopping integral between metal and ligand site increases. This implies that the Chern insulator phase would be difficult to be

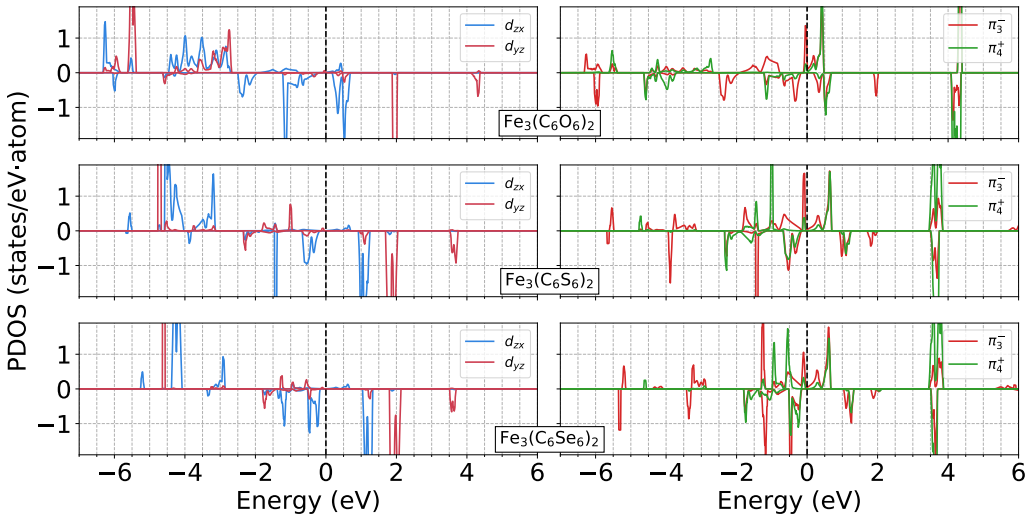

Fig. 6.8. PDOS of $Fe_3(C_6O_6)_2$(top), $Fe_3(C_6S_6)_2$(middle), and $Fe_3(C_6Se_6)_2$ (bottom) system.

observed in $M_3(C_6Se_6)_2$ with this heavy ligand or metal system, and $M_3(C_6S_6)_2$ or $M_3(C_6O_6)_2$ could be a good candidate for realizing the Chern insulator phase.

Chapter 7

Summary and perspectives

In this thesis, we studied the physical properties of a 2D kagome MOFs of M_3L_2-type. This system consists of metal atoms M forming a kagome lattice and organic linkers L connecting metal atoms. We carried out first-principles calculations with various ligands to figure out the common properties of these systems. Five different ligands ($M_3(C_6S_6)_2$, $M_3(C_6O_6)_2$, $M_3(C_6Se_6)_2$, $M_3(HAB)_2$, $M_3(HITP)_2$) were used to check the effects of various ligands. We also constructed a tight-binding model and maximally localized Waannier functions to analyze the detailed electronic properties of the system.

First, we optimized the crystal structure with various ligand types. Regardless of the ligand types, the local geometry near the metal site was similar. The ligands provide a square planar field on metal sites, and the largest energy splitting of metal d orbitals comes from this effect. Among five degenerate d orbitals, d_{z^2} and $d_{x^2-y^2}$ have almost no effects on the magnetic properties because of their low hybridization with ligands. It is verified that d_{zx} and d_{yz} play a vital role in

determining various properties by their large hybridization with ligand p_z orbitals. Also, unlike the oxide system, where oxidation states of the ligand are usually 2^-, two-hole states exist on the ligand site for all cases. This hole state turns out to play an essential role in the determination of the magnetic exchange.

We then calculated total energy to determine the magnetic ground states of M_3L_2 system. It was confirmed that MOFs with V and Cr were in an antiferromagnetic ground state, whereas MOFs with Mn, Fe, and Co were in a ferromagnetic ground state regardless of the ligand types. The primary factor determining the magnetic ground state is the electron occupations on d_{zx} and d_{yz} orbitals. Near the Fermi level, the major orbital components were verified to be d_{zx}, d_{yz}, and p_z orbitals. For V and Cr, spin-up d_{zx} and d_{yz} band is partially occupied, whereas spin-down is empty. Considering the superexchange process between metal sites, the antiferromagnetic exchange is favored in this case. The spin-up band is fully occupied for Mn, Fe, and Co and lies far below Fermi level. Then, only the spin-down band is partially occupied, and ferrimagnetic exchange is favored. This trend is preserved regardless of the ligand types. The dependence of the d electron occupation on the magnetic exchange was also verified by comparing their occupation and total energy trend.

In determining magnetic anisotropy, the spin-orbit coupling on the metal site plays an important role. The magnetic anisotropy affects the determination of the easy axis on the ferromagnetic states. The second-order perturbation theory reveals that d electron occupation affects magnetic anisotropy. Comparing the electron occupation, we determined that Mn and Fe favor out-of-plane magnetization, whereas Co favors in-plane magnetization.

We also observed that the non-trivial band structure could be realized in this

system. $Fe_3(C_6S_6)_2$ and $Mn_3(C_6S_6)_2$ shows that they are Chern insulator for resonable U_{eff} range. They give the Chern number $C = 1$ phase, which was verified by calculating the conducting edge state and anomalous conductance signal. This nontrivial electronic structure arises from the band inversion near the Fermi level. We carried out a tight-binding analysis and verified that the reduction of metal-ligand hybridization is a driving factor in this phase transition.

Throughout the thesis, we have explored the various properties of kagome MOFs, a *new* class of 2D magnetic materials. One can then ask what the advantage of studying this new kind of magnetic materials is over some well-studied materials, such as vdW materials. One benefit of studying MOFs over inorganic compounds would be utilizing the knowledge from organic chemistry. From the perspective of synthesis, much is known to organic compounds than inorganic counterparts. For instance, about 20 million different organic compounds are known, dropping to only 600 thousand for inorganic compounds. Since MOFs are intrinsically composed of inorganic (mostly metal) and organic linkers, MOFs could generate various new kinds of materials. Taking advantage of the bottom-up synthesis technique, which is a good way of achieving a few-layer system, we can also control the layer thickness easily. Another point is chemical stability. Our molecular dynamics and phonon calculations show that the kagome MOFs in our study show high stability over room temperature. This originates from the strong coordination bond between metal and organic linkers. Organic chemistry provides a firm understanding of the bonding nature between metal and organic ligands[108]. We can utilize this knowledge to design stable 2D compounds.

The different bonding nature among d orbitals also provides unique characteristics. Since the magnetic and topological properties are related to the d_{zx} and d_{yz}

states whose robes are headed in an out-of-plane direction, making heterostructure and observing their interlayer coupling could also be an interesting research area. Another degree of freedom is the choice ligand. Even if we only studied five different types of ligands in this thesis, the detailed properties such as bandgap or exchange coupling differ from one to another, and a suitable choice of the ligand could become a way of tuning various properties such as bandwidth, lattice constant, magnetic coupling, or interlayer couplings.

One weakness in studying magnetic MOFs over other materials is the lack of representative compounds. The synthesis of monolayer graphene has opened up the era of 2D material research[1]. VdW mateirals, especially trichalgenides ($NiPS_3$, $FePS_3$ $CrGeTe_3$) and trihalides (CrI_3) have then boosted up the research of magnetic 2D materials[7, 9, 6, 109]. New physics or research trends have always accompanied the discovery of new materials. However, current research on magnetic MOFs lacks such representative materials. Some research reports the observations of magnetic character in MOFs system, but evidence of magnetic ordering and their excitation property is not strong enough.

To overcome this drawback, much research is needed on both theoretical and experimental sides. We need to explore a more diverse area of 2D MOF systems from the theoretical side. In this thesis, we have only dealt with a specific type of MOFs in kagome lattice (M_3L_2). However, High-throughput DFT calculations could screen for a much larger class of 2D MOFs and classify their magnetic ground states and stability. This information could be used as a guide for experimentalists. From the experimental side, we need a more accurate measurement of magnetic properties. Since magnetism is usually ignored in MOFs systems, not many experiments are done on these materials. For instance, Co-based MOFs ($Co_3(HITP)_2$, $Co_3(HAB)_2$)

has been successfully synthesized and their electronic conductivity and reactivity are measured[35, 110]. However, no magnetic properties are measured on these compounds. From our calculations, these compounds also exhibit FM ordering, so as a first step, we need to measure the magnetic properties of known MOFs.

In addition to the conventional inorganic materials, the addition of ligands brings a new degree of freedom in controlling physical properties. As we studied throughout this thesis, these ligands provide various unique characteristics to metal compounds, such as modification of metal bonding characters. 2D MOFs systems, which can be studied by intertwining the knowledge of condensed matter physics and inorganic chemistry, could be another novel playground for studying 2D magnetism.

Bibliography

[1] Andre K Geim and Konstantin S Novoselov. The rise of graphene. In *Nanoscience and technology: a collection of reviews from nature journals*, pages 11–19. World Scientific, 2010.

[2] Unni Krishnan, Manjot Kaur, Kulwinder Singh, Manjeet Kumar, and Akshay Kumar. A synoptic review of mos2: Synthesis to applications. *Superlattices and Microstructures*, 128:274–297, 2019.

[3] Xi Ling, Han Wang, Shengxi Huang, Fengnian Xia, and Mildred S Dresselhaus. The renaissance of black phosphorus. *Proceedings of the National Academy of Sciences*, 112(15):4523–4530, 2015.

[4] Mengqi Zeng, Yao Xiao, Jinxin Liu, Kena Yang, and Lei Fu. Exploring two-dimensional materials toward the next-generation circuits: from monomer design to assembly control. *Chemical reviews*, 118(13):6236–6296, 2018.

[5] Kenneth S Burch, David Mandrus, and Je-Geun Park. Magnetism in two-dimensional van der waals materials. *Nature*, 563(7729):47–52, 2018.

[6] Cheng Gong, Lin Li, Zhenglu Li, Huiwen Ji, Alex Stern, Yang Xia, Ting Cao, Wei Bao, Chenzhe Wang, Yuan Wang, et al. Discovery of intrinsic ferromag-

netism in two-dimensional van der waals crystals. *Nature*, 546(7657):265–269, 2017.

[7] Bevin Huang, Genevieve Clark, Efrén Navarro-Moratalla, Dahlia R Klein, Ran Cheng, Kyle L Seyler, Ding Zhong, Emma Schmidgall, Michael A McGuire, David H Cobden, et al. Layer-dependent ferromagnetism in a van der waals crystal down to the monolayer limit. *Nature*, 546(7657):270–273, 2017.

[8] Feng Xue, Yusheng Hou, Zhe Wang, and Ruqian Wu. Two-dimensional ferromagnetic van der waals crc l 3 monolayer with enhanced anisotropy and curie temperature. *Physical Review B*, 100(22):224429, 2019.

[9] Jae-Ung Lee, Sungmin Lee, Ji Hoon Ryoo, Soonmin Kang, Tae Yun Kim, Pilkwang Kim, Cheol-Hwan Park, Je-Geun Park, and Hyeonsik Cheong. Ising-type magnetic ordering in atomically thin feps3. *Nano letters*, 16(12):7433–7438, 2016.

[10] Yu-Jia Sun, Qing-Hai Tan, Xue-Lu Liu, Yuan-Fei Gao, and Jun Zhang. Probing the magnetic ordering of antiferromagnetic mnps3 by raman spectroscopy. *The Journal of Physical Chemistry Letters*, 10(11):3087–3093, 2019.

[11] Kangwon Kim, Soo Yeon Lim, Jae-Ung Lee, Sungmin Lee, Tae Yun Kim, Kisoo Park, Gun Sang Jeon, Cheol-Hwan Park, Je-Geun Park, and Hyeonsik Cheong. Suppression of magnetic ordering in xxz-type antiferromagnetic monolayer nips3. *Nature Communications*, 10(1):1–9, 2019.

[12] Y Tokunaga, D Okuyama, T Kurumaji, T Arima, H Nakao, Y Murakami, Y Taguchi, and Y Tokura. Multiferroicity in nibr 2 with long-wavelength cy-

cloidal spin structure on a triangular lattice. *Physical Review B*, 84(6):060406, 2011.

[13] T Kurumaji, S Seki, S Ishiwata, H Murakawa, Y Kaneko, and Y Tokura. Magnetoelectric responses induced by domain rearrangement and spin structural change in triangular-lattice helimagnets nii 2 and coi 2. *Physical Review B*, 87(1):014429, 2013.

[14] T Kurumaji, S Seki, S Ishiwata, H Murakawa, Y Tokunaga, Y Kaneko, and Y Tokura. Magnetic-field induced competition of two multiferroic orders in a triangular-lattice helimagnet mni 2. *Physical review letters*, 106(16):167206, 2011.

[15] Dahlia R Klein, David MacNeill, Qian Song, Daniel T Larson, Shiang Fang, Mingyu Xu, Raquel A Ribeiro, Paul C Canfield, Efthimios Kaxiras, Riccardo Comin, et al. Enhancement of interlayer exchange in an ultrathin two-dimensional magnet. *Nature Physics*, 15(12):1255–1260, 2019.

[16] Tiancheng Song, Xinghan Cai, Matisse Wei-Yuan Tu, Xiaoou Zhang, Bevin Huang, Nathan P Wilson, Kyle L Seyler, Lin Zhu, Takashi Taniguchi, Kenji Watanabe, et al. Giant tunneling magnetoresistance in spin-filter van der waals heterostructures. *Science*, 360(6394):1214–1218, 2018.

[17] Davit Ghazaryan, Mark T Greenaway, Zihao Wang, Victor H Guarochico-Moreira, Ivan J Vera-Marun, Jun Yin, Yuanxun Liao, Serge V Morozov, Oleg Kristanovski, Alexander I Lichtenstein, et al. Magnon-assisted tunnelling in van der waals heterostructures based on crbr 3. *Nature Electronics*, 1(6):344–349, 2018.

[18] Kyle L Seyler, Ding Zhong, Dahlia R Klein, Shiyuan Gao, Xiaoou Zhang, Bevin Huang, Efrén Navarro-Moratalla, Li Yang, David H Cobden, Michael A McGuire, et al. Ligand-field helical luminescence in a 2d ferromagnetic insulator. *Nature Physics*, 14(3):277–281, 2018.

[19] Dante J O'Hara, Tiancong Zhu, Amanda H Trout, Adam S Ahmed, Yunqiu Kelly Luo, Choong Hee Lee, Mark R Brenner, Siddharth Rajan, Jay A Gupta, David W McComb, et al. Room temperature intrinsic ferromagnetism in epitaxial manganese selenide films in the monolayer limit. *Nano letters*, 18(5):3125–3131, 2018.

[20] Yuji Yamasaki, Rai Moriya, Miho Arai, Satoru Masubuchi, Sunseng Pyon, Tsuyoshi Tamegai, Keiji Ueno, and Tomoki Machida. Exfoliation and van der waals heterostructure assembly of intercalated ferromagnet cr1/3tas2. *2D Materials*, 4(4):041007, 2017.

[21] Wenyu Xing, Luyi Qiu, Xirui Wang, Yunyan Yao, Yang Ma, Ranran Cai, Shuang Jia, XC Xie, and Wei Han. Magnon transport in quasi-two-dimensional van der waals antiferromagnets. *Physical Review X*, 9(1):011026, 2019.

[22] Benjamin T Zhou, Noah FQ Yuan, Hong-Liang Jiang, and Kam Tuen Law. Ising superconductivity and majorana fermions in transition-metal dichalcogenides. *Physical Review B*, 93(18):180501, 2016.

[23] Dinh Loc Duong, Seok Joon Yun, and Young Hee Lee. van der waals layered materials: opportunities and challenges. *ACS nano*, 11(12):11803–11830, 2017.

[24] Fang Liu, Wenjing Wu, Yusong Bai, Sang Hoon Chae, Qiuyang Li, Jue Wang, James Hone, and X-Y Zhu. Disassembling 2d van der waals crystals into macroscopic monolayers and reassembling into artificial lattices. *Science*, 367(6480):903–906, 2020.

[25] Momoko Onodera, Satoru Masubuchi, Rai Moriya, and Tomoki Machida. Assembly of van der waals heterostructures: exfoliation, searching, and stacking of 2d materials. *Japanese Journal of Applied Physics*, 59(1):010101, 2020.

[26] Meiting Zhao, Ying Huang, Yongwu Peng, Zhiqi Huang, Qinglang Ma, and Hua Zhang. Two-dimensional metal–organic framework nanosheets: synthesis and applications. *Chemical Society Reviews*, 47(16):6267–6295, 2018.

[27] Na Li, Jian Xu, Rui Feng, Tong-Liang Hu, and Xian-He Bu. Governing metal–organic frameworks towards high stability. *Chemical Communications*, 52(55):8501–8513, 2016.

[28] Kuangmin Zhao, Suqin Liu, Guanying Ye, Qingmeng Gan, Zhi Zhou, and Zhen He. High-yield bottom-up synthesis of 2d metal–organic frameworks and their derived ultrathin carbon nanosheets for energy storage. *Journal of Materials Chemistry A*, 6(5):2166–2175, 2018.

[29] MV Varsha and Gomathi Nageswaran. 2d layered metal organic framework nanosheets as an emerging platform for electrochemical sensing. *Journal of the Electrochemical Society*, 167(13):136502, 2020.

[30] Cheng Wang, Demin Liu, and Wenbin Lin. Metal–organic frameworks as a tunable platform for designing functional molecular materials. *Journal of the American Chemical Society*, 135(36):13222–13234, 2013.

[31] Zi'Ang Gao, Yifan Gao, Muqing Hua, Jing Liu, Li Huang, and Nian Lin. Design and synthesis of a single-layer ferromagnetic metal–organic framework with topological nontrivial gaps. *The Journal of Physical Chemistry C*, 124(49):27017–27023, 2020.

[32] Santu Baidya, Seungjin Kang, Choong H Kim, and Jaejun Yu. Chern insulator with a nearly flat band in the metal-organic-framework-based kagome lattice. *Scientific reports*, 9(1):1–8, 2019.

[33] Renhao Dong, Zhitao Zhang, Diana C Tranca, Shengqiang Zhou, Mingchao Wang, Peter Adler, Zhongquan Liao, Feng Liu, Yan Sun, Wujun Shi, et al. A coronene-based semiconducting two-dimensional metal-organic framework with ferromagnetic behavior. *Nature communications*, 9(1):1–9, 2018.

[34] Jihye Park, Minah Lee, Dawei Feng, Zhehao Huang, Allison C Hinckley, Andrey Yakovenko, Xiaodong Zou, Yi Cui, and Zhenan Bao. Stabilization of hexaaminobenzene in a 2d conductive metal–organic framework for high power sodium storage. *Journal of the American Chemical Society*, 140(32):10315–10323, 2018.

[35] Danning Xing, Yuanyuan Wang, Peng Zhou, Yuanyuan Liu, Zeyan Wang, Peng Wang, Zhaoke Zheng, Hefeng Cheng, Ying Dai, and Baibiao Huang. Co3 (hexaiminotriphenylene) 2: A conductive two-dimensional π–d conjugated metal–organic framework for highly efficient oxygen evolution reaction. *Applied Catalysis B: Environmental*, 278:119295, 2020.

[36] Chandrima Chakravarty, Bikash Mandal, and Pranab Sarkar. Bis (dithioline)-based metal–organic frameworks with superior electronic and

magnetic properties: spin frustration to spintronics and gas sensing. *The Journal of Physical Chemistry C*, 120(49):28307–28319, 2016.

[37] Julio Camarero and Eugenio Coronado. Molecular vs. inorganic spintronics: the role of molecular materials and single molecules. *Journal of Materials Chemistry*, 19(12):1678–1684, 2009.

[38] Chao Liu, Kun Zhai, Zhipeng Yu, Anmin Nie, Zhongyuan Liu, and Young Sun. Hydrogen bond tuning of magnetoelectric coupling in metal–organic frameworks. *The Journal of Physical Chemistry C*, 124(29):16111–16115, 2020.

[39] Xingxing Li and Jinlong Yang. Realizing two-dimensional magnetic semiconductors with enhanced curie temperature by antiaromatic ring based organometallic frameworks. *Journal of the American Chemical Society*, 141(1):109–112, 2018.

[40] Menghao Wu, Zhijun Wang, Junwei Liu, Wenbin Li, Huahua Fu, Lei Sun, Xin Liu, Minghu Pan, Hongming Weng, Mircea Dincă, et al. Conetronics in 2d metal-organic frameworks: double/half dirac cones and quantum anomalous hall effect. *2D Materials*, 4(1):015015, 2016.

[41] Peng Wang, Xue Jiang, Jun Hu, Biao Wang, Tingwei Zhou, Hongkuan Yuan, and Jijun Zhao. Robust spin manipulation in 2d organometallic kagome lattices: a first-principles study. *Physical Chemistry Chemical Physics*, 22(19):11045–11052, 2020.

[42] Bohayra Mortazavi, Masoud Shahrokhi, Tanveer Hussain, Xiaoying Zhuang, and Timon Rabczuk. Theoretical realization of two-dimensional m3 (c6x6) 2

(m= co, cr, cu, fe, mn, ni, pd, rh and x= o, s, se) metal–organic frameworks. *Applied Materials Today*, 15:405–415, 2019.

[43] Guillermo Mínguez Espallargas and Eugenio Coronado. Magnetic functionalities in mofs: from the framework to the pore. *Chemical Society Reviews*, 47(2):533–557, 2018.

[44] Eugenio Coronado, Mónica Giménez-Marqués, Guillermo Mínguez Espallargas, and Lee Brammer. Tuning the magneto-structural properties of nonporous coordination polymers by hcl chemisorption. *Nature communications*, 3(1):1–8, 2012.

[45] Guan-Cheng Xu, Wen Zhang, Xiao-Ming Ma, Yi-Hong Chen, Li Zhang, Hong-Ling Cai, Zhe-Ming Wang, Ren-Gen Xiong, and Song Gao. Coexistence of magnetic and electric orderings in the metal–formate frameworks of [nh4][m (hcoo) 3]. *Journal of the American Chemical Society*, 133(38):14948–14951, 2011.

[46] Mario Wriedt, Andrey A Yakovenko, Gregory J Halder, Andrey V Prosvirin, Kim R Dunbar, and Hong-Cai Zhou. Reversible switching from antiferro-to ferromagnetic behavior by solvent-mediated, thermally-induced phase transitions in a trimorphic mof-based magnetic sponge system. *Journal of the American Chemical Society*, 135(10):4040–4050, 2013.

[47] Wei Jiang, Xiaojuan Ni, and Feng Liu. Exotic topological bands and quantum states in metal–organic and covalent–organic frameworks. *Accounts of Chemical Research*, 54(2):416–426, 2021.

[48] Simeng Yan, David A Huse, and Steven R White. Spin-liquid ground state of the s= 1/2 kagome heisenberg antiferromagnet. *Science*, 332(6034):1173–1176, 2011.

[49] Yuki Misumi, Akira Yamaguchi, Zhongyue Zhang, Taku Matsushita, Nobuo Wada, Masahisa Tsuchiizu, and Kunio Awaga. Quantum spin liquid state in a two-dimensional semiconductive metal–organic framework. *Journal of the American Chemical Society*, 142(39):16513–16517, 2020.

[50] Bikash Mandal, Jin Suk Chung, and Sung Gu Kang. Theoretical insight into m1tpyp–m2 (m1, m2= fe, co) mofs: Correlation between electronic structure and catalytic activity extending to potentiality in capturing flue gases. *The Journal of Physical Chemistry C*, 122(18):9899–9908, 2018.

[51] Muqing Hua, Bowen Xia, Miao Wang, En Li, Jing Liu, Tianhao Wu, Yifan Wang, Ruoning Li, Honghe Ding, Jun Hu, et al. Highly degenerate ground states in a frustrated antiferromagnetic kagome lattice in a two-dimensional metal–organic framework. *The Journal of Physical Chemistry Letters*, 12(15):3733–3739, 2021.

[52] T Takenaka, K Ishihara, M Roppongi, Y Miao, Y Mizukami, T Makita, J Tsurumi, S Watanabe, J Takeya, M Yamashita, et al. Strongly correlated superconductivity in a copper-based metal-organic framework with a perfect kagome lattice. *Science Advances*, 7(12):eabf3996, 2021.

[53] Masatoshi Imada, Atsushi Fujimori, and Yoshinori Tokura. Metal-insulator transitions. *Reviews of modern physics*, 70(4):1039, 1998.

[54] Junjiro Kanamori. Superexchange interaction and symmetry properties of electron orbitals. *Journal of Physics and Chemistry of Solids*, 10(2-3):87–98, 1959.

[55] Pierre Hohenberg and Walter Kohn. Inhomogeneous electron gas. *Physical review*, 136(3B):B864, 1964.

[56] Walter Kohn and Lu Jeu Sham. Self-consistent equations including exchange and correlation effects. *Physical review*, 140(4A):A1133, 1965.

[57] Robert Van Leeuwen. Density functional approach to the many-body problem: key concepts and exact functionals. *Adv. Quantum Chem*, 43:25–94, 2003.

[58] Elliott H Lieb. Density functionals for coulomb systems. In *Inequalities*, pages 269–303. Springer, 2002.

[59] H Englisch and R Englisch. Exact density functionals for ground-state energies. i. general results. *physica status solidi (b)*, 123(2):711–721, 1984.

[60] H Englisch and R Englisch. Exact density functionals for ground-state energies ii. details and remarks. *physica status solidi (b)*, 124(1):373–379, 1984.

[61] Myung Joon Han, Taisuke Ozaki, and Jaejun Yu. O (n) lda+ u electronic structure calculation method based on the nonorthogonal pseudoatomic orbital basis. *Physical Review B*, 73(4):045110, 2006.

[62] Matteo Cococcioni and Stefano De Gironcoli. Linear response approach to the calculation of the effective interaction parameters in the lda+ u method. *Physical Review B*, 71(3):035105, 2005.

[63] Heather J Kulik and Nicola Marzari. A self-consistent hubbard u density-functional theory approach to the addition-elimination reactions of hydrocarbons on bare feo+. *The Journal of chemical physics*, 129(13):134314, 2008.

[64] T Ozaki and H Kino. Efficient projector expansion for the ab initio lcao method. *Physical Review B*, 72(4):045121, 2005.

[65] Paolo Giannozzi, Stefano Baroni, Nicola Bonini, Matteo Calandra, Roberto Car, Carlo Cavazzoni, Davide Ceresoli, Guido L Chiarotti, Matteo Cococcioni, Ismaila Dabo, et al. Quantum espresso: a modular and open-source software project for quantum simulations of materials. *Journal of physics: Condensed matter*, 21(39):395502, 2009.

[66] Shuang Chen, Jun Dai, and Xiao Cheng Zeng. Metal–organic kagome lattices m 3 (2, 3, 6, 7, 10, 11-hexaiminotriphenylene) 2 (m= ni and cu): from semiconducting to metallic by metal substitution. *Physical Chemistry Chemical Physics*, 17(8):5954–5958, 2015.

[67] Tianyang Chen, Jin-Hu Dou, Luming Yang, Chenyue Sun, Nicole J Libretto, Grigorii Skorupskii, Jeffrey T Miller, and Mircea Dinca. Continuous electrical conductivity variation in m3 (hexaiminotriphenylene) 2 (m= co, ni, cu) mof alloys. *Journal of the American Chemical Society*, 142(28):12367–12373, 2020.

[68] Eugenio Garribba and Giovanni Micera. The determination of the geometry of cu (ii) complexes: an epr spectroscopy experiment. *Journal of chemical education*, 83(8):1229, 2006.

[69] Nabajit Lahiri, Neda Lotfizadeh, Ryuichi Tsuchikawa, Vikram V Deshpande, and Janis Louie. Hexaaminobenzene as a building block for a family of 2d coordination polymers. *Journal of the American Chemical Society*, 139(1):19–22, 2017.

[70] Bénédicte Garreau-de Bonneval, Kathleen I Moineau-Chane Ching, Fabienne Alary, Thanh-Tuan Bui, and Lydie Valade. Neutral d8 metal bis-dithiolene complexes: Synthesis, electronic properties and applications. *Coordination Chemistry Reviews*, 254(13-14):1457–1467, 2010.

[71] Dawei Feng, Ting Lei, Maria R Lukatskaya, Jihye Park, Zhehao Huang, Minah Lee, Leo Shaw, Shucheng Chen, Andrey A Yakovenko, Ambarish Kulkarni, et al. Robust and conductive two-dimensional metal- organic frameworks with exceptionally high volumetric and areal capacitance. *Nature Energy*, 3(1):30–36, 2018.

[72] Sergei Posysaev, Olga Miroshnichenko, Matti Alatalo, Duy Le, and Talat S Rahman. Oxidation states of binary oxides from data analytics of the electronic structure. *Computational Materials Science*, 161:403–414, 2019.

[73] Indrani Choudhuri and Donald G Truhlar. Calculating and characterizing the charge distributions in solids. *Journal of Chemical Theory and Computation*, 16(9):5884–5892, 2020.

[74] Jin-Hu Dou, Lei Sun, Yicong Ge, Wenbin Li, Christopher H Hendon, Ju Li, Sheraz Gul, Junko Yano, Eric A Stach, and Mircea Dinca. Signature of metallic behavior in the metal–organic frameworks m3 (hexaiminobenzene) 2 (m= ni, cu). *Journal of the American Chemical Society*, 139(39):13608–13611, 2017.

[75] George C Papavassiliou, George C Anyfantis, and George A Mousdis. Neutral metal 1, 2-dithiolenes: preparations, properties and possible applications of unsymmetrical in comparison to the symmetrical. *Crystals*, 2(3):762–811, 2012.

[76] Sebastien Blanchard, Frank Neese, Eberhard Bothe, Eckhard Bill, Thomas Weyhermüller, and Karl Wieghardt. Square planar vs tetrahedral coordination in diamagnetic complexes of nickel (ii) containing two bidentate π-radical monoanions. *Inorganic chemistry*, 44(10):3636–3656, 2005.

[77] Karim Essafi, Owen Benton, and LDC Jaubert. Generic nearest-neighbor kagome model: Xyz and dzyaloshinskii-moriya couplings with comparison to the pyrochlore-lattice case. *Physical Review B*, 96(20):205126, 2017.

[78] Karim Essafi, Owen Benton, and Ludovic DC Jaubert. A kagome map of spin liquids from xxz to dzyaloshinskii–moriya ferromagnet. *Nature communications*, 7(1):1–7, 2016.

[79] Owen Benton. Ordered ground states of kagome magnets with generic exchange anisotropy. *Physical Review B*, 103(17):174425, 2021.

[80] O Götze and J Richter. Ground-state phase diagram of the xxz spin-s kagome antiferromagnet: A coupled-cluster study. *Physical Review B*, 91(10):104402, 2015.

[81] Michael E Zhitomirsky. Octupolar ordering of classical kagome antiferromagnets in two and three dimensions. *Physical Review B*, 78(9):094423, 2008.

[82] Sergey V Streltsov and Daniel I Khomskii. Orbital physics in transition metal compounds: new trends. *Physics-Uspekhi*, 60(11):1121, 2017.

[83] Pratibha Dev, Yu Xue, and Peihong Zhang. Defect-induced intrinsic magnetism in wide-gap iii nitrides. *Physical review letters*, 100(11):117204, 2008.

[84] Priya Mahadevan, Alex Zunger, and D Das Sarma. Unusual directional dependence of exchange energies in gaas diluted with mn: is the rkky description relevant? *Physical review letters*, 93(17):177201, 2004.

[85] Wei Jiang, Zheng Liu, Jia-Wei Mei, Bin Cui, and Feng Liu. Dichotomy between frustrated local spins and conjugated electrons in a two-dimensional metal–organic framework. *Nanoscale*, 11(3):955–961, 2019.

[86] Jennifer C Green, Andrew L Hector, Anthony F Hill, Sibo Lin, and James DET Wilton-Ely. Synthetic and computational studies of thiocarbonyl/σ-organyl coupling reactions. *Organometallics*, 27(21):5548–5558, 2008.

[87] Ding-sheng Wang, Ruqian Wu, and AJ Freeman. First-principles theory of surface magnetocrystalline anisotropy and the diatomic-pair model. *Physical Review B*, 47(22):14932, 1993.

[88] Kai Sun, Zhengcheng Gu, Hosho Katsura, and S Das Sarma. Nearly flatbands with nontrivial topology. *Physical review letters*, 106(23):236803, 2011.

[89] DN Sheng, Zheng-Cheng Gu, Kai Sun, and L Sheng. Fractional quantum hall effect in the absence of landau levels. *Nature communications*, 2(1):1–5, 2011.

[90] Jun-Won Rhim and Bohm-Jung Yang. Singular flat bands. *Advances in Physics: X*, 6(1):1901606, 2021.

[91] Yosuke Nagaoka. Ferromagnetism in a narrow, almost half-filled s band. *Physical Review*, 147(1):392, 1966.

[92] Hal Tasaki. From nagaoka's ferromagnetism to flat-band ferromagnetism and beyond: an introduction to ferromagnetism in the hubbard model. *Progress of theoretical physics*, 99(4):489–548, 1998.

[93] Jing-Yang You, Bo Gu, and Gang Su. Flat band and hole-induced ferromagnetism in a novel carbon monolayer. *Scientific reports*, 9(1):1–7, 2019.

[94] Evelyn Tang and Liang Fu. Strain-induced partially flat band, helical snake states and interface superconductivity in topological crystalline insulators. *Nature Physics*, 10(12):964–969, 2014.

[95] Shintaro Takayoshi, Hosho Katsura, Noriaki Watanabe, and Hideo Aoki. Phase diagram and pair tomonaga-luttinger liquid in a bose-hubbard model with flat bands. *Physical Review A*, 88(6):063613, 2013.

[96] GE Volovik. Graphite, graphene, and the flat band superconductivity. *JETP Letters*, 107(8):516–517, 2018.

[97] Hiroyuki Tajima, Pierbiagio Pieri, and Andrea Perali. Hidden pseudogap and excitation spectra in a strongly coupled two-band superfluid/superconductor. *Condensed Matter*, 6(1):8, 2021.

[98] Zhen Zhang, Jing-Yang You, Xing-Yu Ma, Bo Gu, and Gang Su. Kagome quantum anomalous hall effect with high chern number and large band gap. *Physical Review B*, 103(1):014410, 2021.

[99] An Zhao and Shun-Qing Shen. Quantum anomalous hall effect in a flat band ferromagnet. *Physical Review B*, 85(8):085209, 2012.

[100] Biplab Pal and Kush Saha. Flat bands in fractal-like geometry. *Physical Review B*, 97(19):195101, 2018.

[101] Atanu Nandy. Controlled imprisonment of wave packet and flat bands in a fractal geometry. *Physica Scripta*, 96(4):045802, 2021.

[102] Congjun Wu, Doron Bergman, Leon Balents, and S Das Sarma. Flat bands and wigner crystallization in the honeycomb optical lattice. *Physical review letters*, 99(7):070401, 2007.

[103] Yuanping Chen, Shenglong Xu, Yuee Xie, Chengyong Zhong, Congjun Wu, and SB Zhang. Ferromagnetism and wigner crystallization in kagome graphene and related structures. *Physical Review B*, 98(3):035135, 2018.

[104] Błażej Jaworowski, Alev Devrim Güçlü, Piotr Kaczmarkiewicz, Michał Kupczyński, Paweł Potasz, and Arkadiusz Wójs. Wigner crystallization in topological flat bands. *New Journal of Physics*, 20(6):063023, 2018.

[105] Charles L Kane and Eugene J Mele. Quantum spin hall effect in graphene. *Physical review letters*, 95(22):226801, 2005.

[106] N David Mermin and Herbert Wagner. Absence of ferromagnetism or antiferromagnetism in one-or two-dimensional isotropic heisenberg models. *Physical Review Letters*, 17(22):1133, 1966.

[107] Robert K Szilagyi, Booyong S Lim, Thorsten Glaser, Richard H Holm, Britt Hedman, Keith O Hodgson, and Edward I Solomon. Description of the ground state wave functions of ni dithiolenes using sulfur k-edge x-ray absorption spectroscopy. *Journal of the American Chemical Society*, 125(30):9158–9169, 2003.

[108] Benjamin J Frogley, Anthony F Hill, and Lachlan J Watson. Advances in transition metal seleno-and tellurocarbonyl chemistry. *Chemistry–A European Journal*, 26(56):12706–12716, 2020.

[109] Soonmin Kang, Kangwon Kim, Beom Hyun Kim, Jonghyeon Kim, Kyung Ik Sim, Jae-Ung Lee, Sungmin Lee, Kisoo Park, Seokhwan Yun, Taehun Kim, et al. Coherent many-body exciton in van der waals antiferromagnet nips3. *Nature*, 583(7818):785–789, 2020.

[110] Chun Li, Lingling Shi, Lili Zhang, Peng Chen, Junwu Zhu, Xin Wang, and Yongsheng Fu. Ultrathin two-dimensional π–d conjugated coordination polymer co 3 (hexaaminobenzene) 2 nanosheets for highly efficient oxygen evolution. *Journal of Materials Chemistry A*, 8(1):369–379, 2020.

국문 초록

이차원 물질의 연구는 실험기술의 발전과 함께 급속한 발전을 이루었다. 다양한 이차원 물질의 후보군들 중, 금속유기화합물은 최근들어 이차원 성질을 연구하기에 적절한 물질군으로 새롭게 평가받고 있다. 이미 화학적으로 잘 알려진 유기물들의 성질을 활용해 원하는 물질의 성질을 조절할 수 있는 것이 금속유기화합물의 장점 중 하나이다. 몇몇 카고메 구조를 가지는 물질군에서는 이미 강자성, 스핀류, 양자 홀 효과 같은 현상들이 보고되어 있다. 하지만 자성을 가지는 금속유기화합물을 설계하는 것은 일반적으로 어려운 일인데, 같은 금속이라도 리간드의 선택에 따라 자성이 쉽게 변하기 때문이다. 또한 목표로 하는 물질의 특성에 따라 적절한 리간드를 선택하는 과정또한 필요하다. 따라서, 금속유기화합물에 관한 연구를 더 진행하기위해서는 해당 물질의 일반적인 전자구조와 자성에 관한 이해가 필요한 시점이다..

본 연구에서는 이차원 카고메 격자형태를 가지는 금속유기화합물의 전자, 자기, 위상적인 특징을 이해할 수 있는 이론을 제시한다. 제일원리계산을 통하여 금속 및 리간드의 종류에 따라 해당 물질의 구조, 자화상태, 위상학적 성질이 어떻게 변하는지를 계산하였다. 금속과 리간드의 결합상태가 특히나 이 물질의 여러 성질을 결정하는 요소들 중 가장 중요한 요소임을 밝히고 자화의 원리또한 제시한다. 위상학적 성질 또한 금속과 리간드의 결합에 크게 의존하게 되는데, 어떻게 이것을 조절 할 수 있는지 제시한다.